

## A simple model for the emergence of relaxation-oscillator convection

FRANCISCO E. SPAULDING-ASTUDILLO <sup>1</sup> AND JONATHAN L. MITCHELL <sup>1,2</sup>

<sup>1</sup>*Department of Earth, Planetary, and Space Sciences, University of California, Los Angeles  
595 Charles E Young Dr E, Los Angeles, CA 90095, USA*

<sup>2</sup>*Department of Atmospheric and Oceanic Sciences, University of California, Los Angeles  
520 Portola Plaza, Los Angeles, CA 90095, USA*

Submitted to *AGU Advances*

### ABSTRACT

Earth’s tropics are characterized by quasi-steady precipitation with small oscillations about a mean value, which has led to the hypothesis that moist convection is in a state of quasi-equilibrium (QE). In contrast, very warm simulations of Earth’s tropical convection are characterized by relaxation-oscillator-like (RO) precipitation, with short-lived convective storms and torrential rainfall forming and dissipating at regular intervals with little to no precipitation in between. We develop a model of moist convection by combining a zero-buoyancy model of bulk-plume convection with a QE heat engine model, and we use it to show that QE is violated at high surface temperatures. We hypothesize that the RO state emerges when the equilibrium condition of the convective heat engine is violated, i.e., when the net cooling times a thermodynamic efficiency exceeds the work that can be performed. We test our hypothesis against one- and three-dimensional numerical simulations and find that it accurately predicts the onset of RO convection. The proposed mechanism for RO emergence from QE breakdown is agnostic of the condensing component, and can be applied to any planetary atmosphere undergoing moist convection. To date, RO states have only been demonstrated in three-dimensional convection-resolving simulations, which has made it seem that the physics of the RO state requires simulations that can explicitly resolve the three-dimensional interaction of cloudy plumes and their environment. We demonstrate that RO states also exist in single-column simulations of radiative-convective equilibrium with parameterized convection, albeit in a different surface temperature range and with much longer storm-free intervals.

*Keywords:* Atmospheric dynamics (2300) — Planetary climates (2184) — Atmospheric clouds (2180)

### 1. INTRODUCTION

To investigate the nature of convective dynamics in moist planetary atmospheres under varying conditions, we often rely on numerical climate models. These models are differentiated by whether or not they resolve convective processes, which refers to vertical motion at the scale of individual clouds (“plumes”). Models that can resolve convection are known to simulate the climate more realistically, but can be computationally expensive to run over very large domains. In coarse-resolution climate models that simulate the three-dimensional structure of the atmosphere on regional or global scales, parameterizations are employed to represent the net (“bulk”) effect of an ensemble of unresolved plumes that turbulently mix with the surrounding environment. The bulk-plume representation of convection relates the properties of the plume ensemble (consisting of numerous members of varying size and intensity) to the large-scale radiative forcing through the concept of quasi-equilibrium (QE; [Arakawa & Schubert 1974](#); [Emanuel 2001](#)). QE is, by definition, a *hypothesis* that there exists a steady balance between generation and dissipation of kinetic energy in convecting atmospheres ([Yano & Plant 2012](#)). The QE hypothesis has been invoked successfully in various contexts, for example, to reveal the dynamics of mature hurricanes ([Emanuel 1986, 2001](#)), formulate scaling laws for the maximum intensity of convective storms ([Emanuel & Bister 1996](#)), derive analytical solutions for the large-scale tropical circulation ([Neelin & Zeng 2000](#)), and resolve the closure problem in the bulk-plume parameterization of convection ([Arakawa &](#)

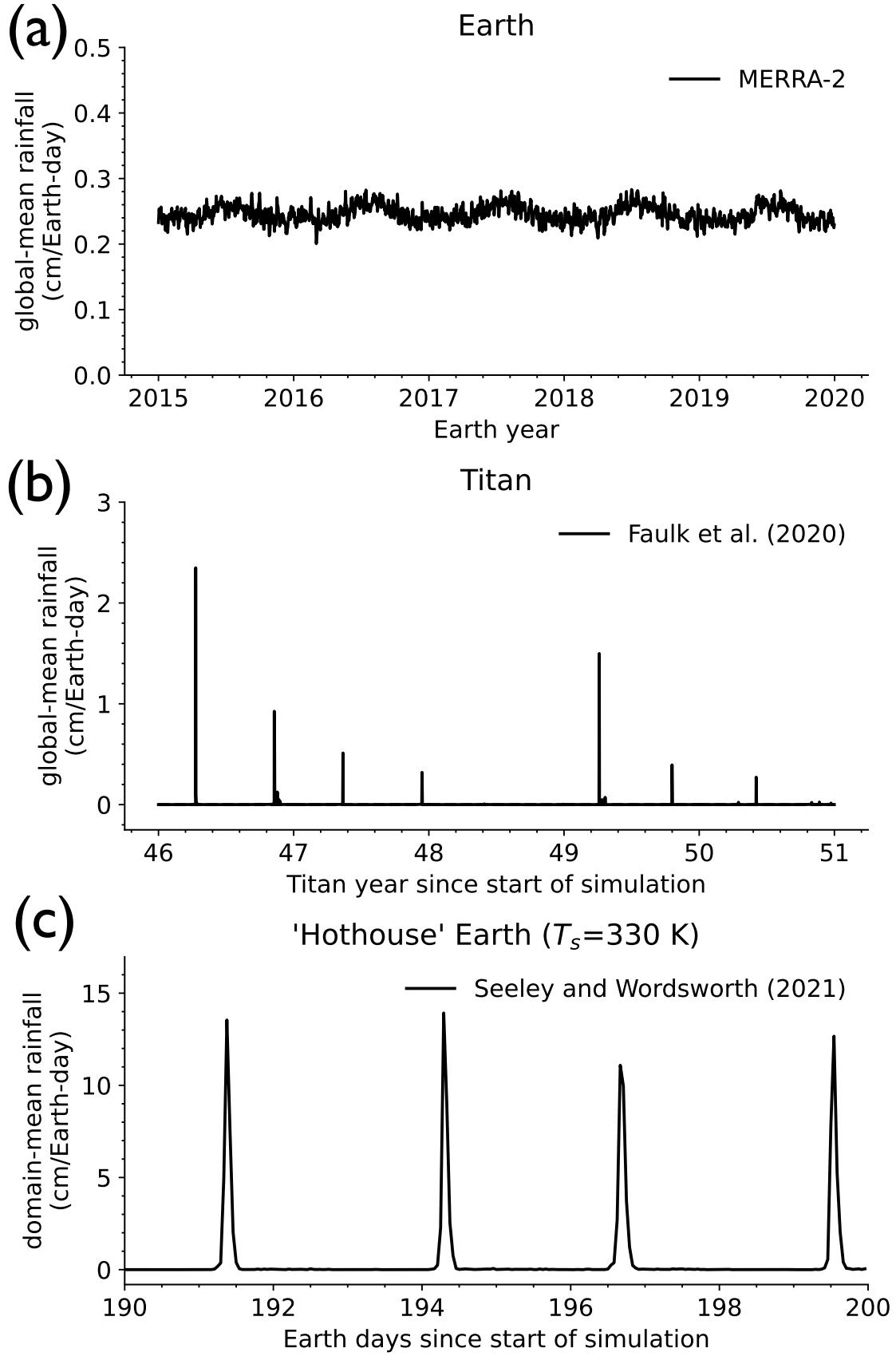


**Figure 1.** Comparison of global-mean precipitation on (a) Earth from the MERRA-2 Earth climate reanalysis and (b) Titan from Titan Atmospheric Model simulations with best-fit land surface hydrology from [Faulk et al. \(2020\)](#), respectively. In (c), we show the domain-averaged precipitation in convection-resolving model aquaplanet simulations of the “Hothouse Earth” at a surface temperature of 330 K from [Seeley & Wordsworth \(2021a\)](#).

Schubert 1974).<sup>1</sup> Thus, while the precise range of states over which QE is valid remains unclear (Yano & Plant 2012), its utility in advancing conceptual understanding of moist convection is evident.

In the contemporary solar system, there are two planets with similar atmospheric compositions but distinct convective dynamics: Earth and Saturn’s moon Titan. Their atmospheres are nitrogen-dominated, and each has a condensing component that participates in an important “hydrological” cycle, i.e. the condensable undergoes phase changes to form clouds and precipitation (Hörsst 2017). Whereas the condensing component on Earth is obviously water, the atmosphere of Titan is so cold that methane (and to a lesser extent nitrogen) condenses (Mitchell & Lora 2016; Tokano 2017) while water is part of the icy bedrock of the Titan’s surface (Griffith et al. 2003). The pattern of global-mean precipitation on Earth (Figure 1a) from the MERRA-2 global climate reanalysis and Titan (Figure 1b) from global simulations of Titan by Faulk et al. (2020) reveals important differences in their hydrological cycles. On Earth, global-mean precipitation is quasi-steady about a mean value with small oscillations (Figure 1a), suggesting that modern Earth has QE-type convection. On Titan, however, rain is the exception, rather than the rule (Figure 1b); storms erupt at semi-regular intervals with vigorous, short-lived rainfall of several centimeters per Earth day and extended dry spells in between (Battaglio et al. 2022). The largest observed storms produce cloud cover up to 10% of Titan’s disk, in contrast to most observations showing very little cloud cover (Griffith et al. 1998; Schaller et al. 2009). During these storms (Dhingra et al. 2019; Turtle et al. 2011), Titan’s surface is likely subject to fluvial erosion which carves out channels and valleys and discharges the sediments into alluvial fans (Perron et al. 2006; Hörsst 2017; Faulk et al. 2017; Lewis-Merrill et al. 2022).

Where does this striking difference in surface precipitation originate? In this study, we take the first step towards answering that question by taking a holistic view of the role of moisture in radiative-convective processes. For completeness, we begin with some background on the physics of moist convection as it relates to convective storms. The temperature of a moist air parcel decreases less rapidly with height than a dry air parcel displaced from the same initial location because of latent heat release. If the moist parcel is displaced adiabatically<sup>2</sup> above its saturation level, then it is usually warmer than the sub-saturated environment in which it is embedded, and therefore accelerates upward due to buoyancy,<sup>3</sup> condensing water along its path. The vertical integral of positive buoyancy  $B$  ( $\text{m/s}^2$ ) along the upward trajectory of an adiabatic parcel is known as the convective available potential energy (CAPE;  $\text{Jkg}^{-1}$ ):

$$\text{CAPE} = \int_{\text{LCL}}^{\text{LNB}} \max(0, B) dz, \quad (1)$$

where LCL is the lifting condensation level and LNB is the level of neutral buoyancy. CAPE is an important meteorological quantity because it represents the maximum intensity of convective storms and is, for example, correlated with the frequency distribution of lightning flashes on Earth (Romps et al. 2018). Energetically, Equation 1 represents the total work done by the environment in lifting the adiabatic parcel from the LCL to the LNB. CAPE measures the buoyancy that is generated by the absorption of solar radiation at the surface and emission of planetary radiation to space in the troposphere, and represents the “fuel” for thunderstorms. Coincidentally, regions of Titan with elevated near-surface humidity ( $\sim 60\%$ ) have similar values of CAPE to the modern-day tropics of Earth (Griffith et al. 2008; Tokano et al. 2006; Barth & Rafkin 2007; Seeley & Wordsworth 2023), indicating the potential for intense storms and rainfall.

It has recently come to light that there is an emergent *dynamical similarity* between contemporary Titan and a hotter Earth (Figure 1b,c). The key discovery, in this case, was made by Seeley & Wordsworth (2021a) in a study of Earth’s tropical clouds and precipitation, in which the authors incrementally increased the surface temperature in a convection-resolving model. At surface temperatures above 320 K, they discovered a “hothouse” climate state with a new mode of convection undergoing relaxation oscillations. The convective oscillations produced deluges lasting a few hours that then repeated every few days (Figure 1c). Unlike modern Earth, hothouse (often referred to as “moist greenhouse”) climate simulations have radiative heating in the lower troposphere (Wolf & Toon 2015). Seeley & Wordsworth (2021a) hypothesized this lower-tropospheric radiative heating (LTRH) is a necessary condition for the RO state. LTRH occurs in hothouse climates because of the thermodynamic and radiative properties of water vapor. Around 320 K, the “water vapor window” - a spectral region over which the present-day atmosphere is transparent

<sup>1</sup> The definition of quasi-equilibrium has varied over time and between contexts, as is elegantly described in a review article by Yano & Plant (2012).

<sup>2</sup> An adiabatic parcel does not exchange mass or heat with its surroundings.

<sup>3</sup> The low molecular weight of water vapor on Earth and methane vapor on Titan relative to the dry background gases (Seidel & Yang 2020; Mitchell & Lora 2016) lends additional buoyancy to moist parcels of air (Yang & Seidel 2020).

to infrared radiation (Pierrehumbert 2010) - closes (Koll & Cronin 2018) due to increases in the atmospheric opacity, which prevents the lower atmosphere from directly cooling to space (Wolf & Toon 2015). Seeley & Wordsworth (2021a) tested the LTRH hypothesis by carrying out a series of experiments with fixed radiative cooling profiles with and without LTRH. In cases with imposed LTRH, RO states emerged at much lower temperatures close to the modern-day tropics ( $\sim 290$  K). In cases without LTRH, no RO states emerged. Two subsequent studies found that the RO state can emerge even in the absence of LTRH (Dagan et al. 2023; Song et al. 2023). Given the available evidence, it is unclear whether LTRH drives RO emergence or has a strong association with it.

There is a consensus among the aforementioned studies that water vapor plays an important role in the emergence of RO convection at high temperatures on Earth. In what follows, we explore the nature of that role. In QE convection, kinetic energy is generated and dissipated in the atmosphere at equal rates, conceivably leading to steady precipitation. Since the RO state is, by definition, non-steady, it suggests that we may conceive of the QE-to-RO transition as a *breakdown of quasi-equilibrium*. To look for a breakdown of QE convection with increasing surface temperature (and/or, as we will see, moisture content), what is needed is a plausible model of QE convection. Since the atmosphere is a compressible system, parcels/plumes exchange energy with the environment through heat exchange and work, the simplest QE model of convection is that of a heat engine (Rennó & Ingersoll 1996; Emanuel & Bister 1996) defined in the traditional way as any closed system that converts heat into work at some thermodynamic efficiency. In the context of an atmosphere, the work done by the convective heat engine is known as CAPE and heat is transferred to and from the system in the form of radiation (Arakawa & Schubert 1974; Emanuel 1986).

The dynamical similarity of Titan and the hothouse Earth (Figure 1a,c) could point to an underlying physical mechanism that is general to both planets, and their example motivates us to search for an explanation that is inclusive of both radiative and convective processes. A heat engine theory of convection would be agnostic of the atmospheric composition and the condensing substance. For this reason, it is an ideal framework to compare the atmospheres of Earth and Titan. While a goal for future work is to establish whether the theory can explain Titan's bursty methane precipitation (Figure 1b), the specific aim of this study is to apply the theory to Earth.

## 2. THEORY

The QE state is characterized by a steady balance between the generation of CAPE by radiation and its conversion into kinetic energy - i.e., convective motion. The RO state is clearly not steady, however we hypothesize that exploring the conditions in which the steady, QE state is valid can illuminate the mechanisms that lead to the transition from QE to RO convection. First, we construct a quasi-equilibrium model of a convective heat engine (Section 2.1; Emanuel & Bister 1996) in which entraining clouds have zero-buoyancy relative to their local environment (Section 2.2; Singh & O'Gorman 2013; Romps 2016). Second, we demonstrate that QE-type convection is inconsistent with the energetic requirements of radiative-convective equilibrium when the surface is sufficiently warm and/or humid (Section 2.3). Thus, we predict that RO-type convection emerges in warm and humid conditions.

### 2.1. Theory 1: convection as a heat engine

Here, we summarize a quasi-equilibrium model of convection developed by Emanuel & Bister (1996). We begin with the specific entropy ( $s$ ;  $\text{J kg}^{-1} \text{K}^{-1}$ ) budget of the climate system (defined as the surface and the atmosphere) as described by Singh & O'Neill (2022):

$$\frac{\partial s}{\partial t} = \dot{s}_{rad} + \dot{s}_{irr} \quad (2)$$

where  $\dot{s}_{rad} < 0$  is the entropy change associated with radiative processes and  $\dot{s}_{irr} > 0$  is the entropy change associated with irreversible processes within the climate system. Since Earth receives low entropy energy from the sun and releases high entropy energy to space, radiative processes represent a sink of entropy (Singh & O'Neill 2022). Dry processes such as dissipation of convective turbulence and moist processes such as re-evaporation and hydrometeor sedimentation irreversibly increase the entropy of the climate system (Singh & O'Neill 2022). Following Emanuel & Bister (1996), we assume that the climate system is sufficiently close to equilibrium that the sources and sinks of entropy are in statistical balance. Taking the average of the entropy budget over space and time (represented by brackets), following Singh & O'Neill (2022),

$$\langle \dot{s}_{rad} \rangle = \langle \dot{s}_{irr} \rangle, \quad (3)$$

this argument of statistical balance is clear. In a dry atmosphere, the dominant irreversible source of entropy on the right-hand side of Equation 3 is dissipation of convective turbulence. This key assumption of the heat engine model

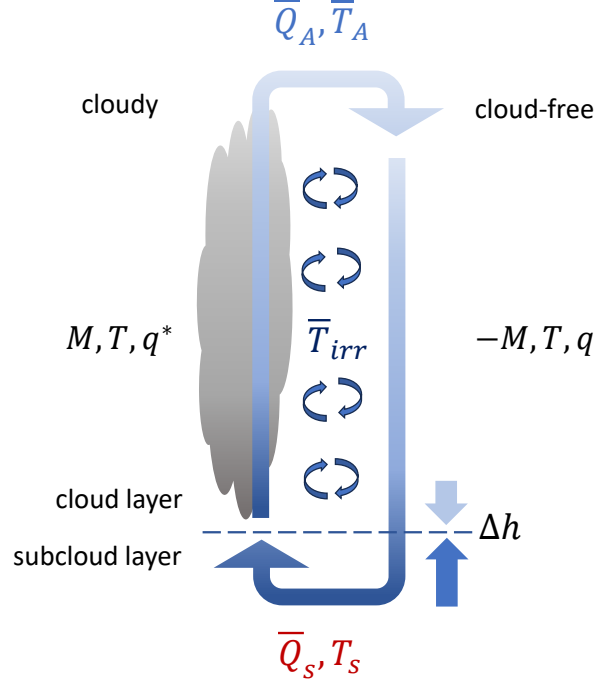


**Figure 2.** Schematic illustration of the zero-buoyancy heat engine model of convection based on Emanuel & Bister (1996) and Romps (2016). Heat in the form of radiation is absorbed at the warm surface temperature  $T_s$  at a rate  $\overline{Q}_s$  and emitted at the cold radiating temperature  $T_A$  at a rate  $\overline{Q}_A$ . The mass flux  $M$  is assumed to be constant with height as well as equal and opposite between ascending cloudy and descending cloud-free regions, which are permitted to turbulently mix. The rate of work is  $M \times \text{CAPE}$ . Heat is converted into work at a thermodynamic efficiency  $\eta$  that is a ratio of the temperatures at which convective turbulence is irreversibly dissipated ( $\overline{T}_{irr}$ ) and radiation is absorbed and emitted. In the zero-buoyancy approximation, cloudy regions and cloud-free regions have the same temperature  $T$  but different specific humidities at each height. In statistical equilibrium, mixing equal parts of air between the cloud layer and subcloud layer implies a net upward transport of moist static energy ( $\Delta h$ ).

allows radiative and convective processes to be directly related.<sup>4</sup> The caveats of this approach are addressed in Section 5 and at greater length by Singh & O’Neill (2022) and Emanuel & Bister (1996). The mass-integrated radiative cooling of the atmosphere ( $\overline{Q}_A$ ;  $\text{Wm}^{-2}$ ) balances surface heating ( $\overline{Q}_s$ ;  $\text{Wm}^{-2}$ ) in equilibrium:

$$\overline{Q}_s + \overline{Q}_A = 0, \quad (4)$$

where bars denote mass-weighted averages. The surface radiative heating is

$$\overline{Q}_s = SW_{toa} - \Delta SW - LW_0, \quad (5)$$

where  $SW_{toa}$  is the net downward solar radiation at the top of the atmosphere,  $\Delta SW$  is the solar radiation absorbed in the atmosphere, and  $LW_0$  is the net upward longwave radiation at the surface. The atmospheric radiative cooling is

$$\overline{Q}_A = LW_0 + \Delta SW - LW_{toa}, \quad (6)$$

where  $LW_{toa}$  is the net upward longwave radiation at the top of the atmosphere. Radiative processes are assumed to be thermodynamically reversible where absorption and emission occur at a mean temperature of  $T_s$  and  $\overline{T}_A$ . The sink of specific entropy associated with radiative processes is

$$\frac{1}{g} \int_V \left( \frac{\partial s}{\partial t} \right)_{rev} dp = \frac{\overline{Q}_s}{T_s} + \frac{\overline{Q}_A}{\overline{T}_A} = \overline{Q}_A \left( \frac{1}{T_s} - \frac{1}{\overline{T}_A} \right), \quad (7)$$

<sup>4</sup> A thorough discussion of the dry and moist processes in Earth’s entropy budget can be found in Singh & O’Neill (2022). The relative importance of these processes as a function of surface temperature has not been established. Though wrong to a certain extent, the assumption that mechanical dissipation dominates is therefore a logical starting place and, moreover, may more accurately capture the behavior of climate models which often neglect moist sources of entropy generation.

where

$$1/\bar{T}_A = \frac{\int_V Q_A/T \, dp/g}{\int_V Q_A \, dp/g}, \quad (8)$$

and the subscript “V” indicates an integral over the volume of the system. Next, we assume that the only source of entropy in the system is the dissipation of kinetic energy in convective turbulence. Invoking quasi-equilibrium, the vertical integral of the “kinetic energy equation” - that is, the equation describing the time rate of change of kinetic energy per unit volume - is a balance between pressure work and dissipation:

$$\int_V [-v \cdot \nabla p + \rho f \cdot v] = 0, \quad (9)$$

where  $v$  is the velocity,  $p$  is the pressure,  $f$  is the net frictional acceleration and  $\rho$  is density. We refer to the first term in the above equation as “pressure work” and the second as “dissipation”. The units of these terms are  $\text{Wm}^{-3}$ . Dissipation is an irreversible source of entropy; assuming it occurs at an average temperature  $\bar{T}_{irr}$ ,

$$\frac{1}{g} \int_V \left( \frac{\partial s}{\partial t} \right)_{irr} dp = -\frac{1}{\bar{T}_{irr}} \int_V \rho f \cdot v \quad (10)$$

Emanuel & Bister (1996) show that to a good approximation

$$\int_V -v \cdot \nabla p \approx \int_V MB, \quad (11)$$

where  $M$  is the mass flux and

$$B = g \frac{(\rho - \rho')}{\rho'} \quad (12)$$

is the buoyancy,  $\rho$  is the density of the environment, and  $\rho'$  is the density of the working fluid (i.e. the parcel/plume);  $MB$  is the buoyancy flux ( $\text{Wm}^{-3}$ ). The above imply the dissipation is equal to the buoyancy flux. Strictly speaking, the buoyancy flux sums over the updrafts and the downdrafts. We neglect the effect of downdrafts by assuming that descending parcels are pegged to the local environmental density, meaning that updrafts are the only source of pressure work. We leave the study of downdrafts to future work. Therefore, the irreversible source of entropy is

$$\frac{1}{g} \int_V \left( \frac{\partial s}{\partial t} \right)_{irr} dp = \frac{1}{\bar{T}_{irr}} \int_V MB, \quad (13)$$

In equilibrium, the net change in entropy is zero (Equation 3), so the sinks and sources must balance:

$$\bar{Q}_A \left( \frac{1}{\bar{T}_s} - \frac{1}{\bar{T}_A} \right) = -\frac{1}{\bar{T}_{irr}} \int_V MB. \quad (14)$$

If we assume the mass flux is constant, as would be approximately true for an adiabatic plume,

$$M \int_V B = M \times \text{CAPE}. \quad (15)$$

CAPE is the convective available potential energy, i.e. the part of the potential energy that is available to convert to kinetic energy. Summarizing the above, the heating due to frictional dissipation of convective turbulence is substituted for the buoyancy flux in quasi-equilibrium, which we results in a direct proportionality between the entropy source and the rate of mechanical work. Defining the thermodynamic efficiency,

$$\eta = -\bar{T}_{irr} \left( \frac{1}{\bar{T}_s} - \frac{1}{\bar{T}_A} \right), \quad (16)$$

and substituting Equations 15 and 16 into Equation 14, we arrive at

$$\eta \bar{Q}_A = M \times \text{CAPE}. \quad (17)$$

The above equation can be thought of as representing a convecting atmosphere as a heat engine in quasi-equilibrium. The engine is cooled at a rate  $\overline{Q}_A$ , but is not perfectly efficient and therefore does work at a rate  $M \times \text{CAPE}$ . Solving for the mass flux implied by the convective heat engine,<sup>5</sup>

$$M = \frac{\eta \overline{Q}_A}{\text{CAPE}}. \quad (18)$$

### 2.1.1. The subcloud mass flux in radiative-convective equilibrium

Following Emanuel & Bister (1996), we divide the system into a subcloud layer and a cloud layer. In the two-layer model, the cooling rate sums over both layers of the atmosphere:

$$\overline{Q}_A = \overline{Q}_{A,sc} + \overline{Q}_{A,cl} \quad (19)$$

The energy budget of the subcloud layer in radiative-convective equilibrium allows us to estimate the mass flux therein:

$$\overline{Q}_s + \overline{Q}_{A,sc} + M_{sc}(h_{cl} - h_{sc}) = 0. \quad (20)$$

Here the subscript “sc” indicates the subcloud layer, the subscript “cl” indicates the cloud layer, and  $h = c_p T + gz + Lq$  is the moist static energy (MSE). Mixing equal parts of air between the two layers implies a net upward transport of MSE. Following Emanuel & Bister (1996), we assume that the air parcels representative of the sub-cloud layer originate near the surface and those representative of the cloud layer originate near the tropospheric minimum in MSE,<sup>6</sup> and are exchanged across the LCL. If the parcels conserve their MSE, the two-layer MSE difference is

$$\begin{aligned} \Delta h &= h_{sc} - h_{cl} \\ &= \Delta(c_p T) + \Delta(gz) + \Delta(Lq) \\ &\approx c_p(T_s - T_{min}) + g(z_s - z_{min}) + L(q_s - q_{min}) \end{aligned} \quad (21)$$

where the subscript “s” indicates the near-surface, the subscript “min” indicates the tropospheric minimum in MSE,  $\Delta(c_p T) + \Delta(gz)$  is the dry static energy difference, and  $\Delta(Lq)$  is the latent energy difference. Substituting Equations 4 and 19 into Equation 20, we solve for the mass flux from the sub-cloud layer:

$$M_{sc} = \frac{\overline{Q}_{A,cl}}{\Delta h} \approx \frac{\overline{Q}_A}{\Delta h} \quad (22)$$

It is clear that the role of convection in radiative-convective equilibrium is to re-distribute latent and sensible heat. We assume that cooling rates are small in the subcloud layer such that  $\overline{Q}_{A,cl} \approx \overline{Q}_A$ .<sup>7</sup> The approximate form of  $M_{sc}$  (Equation 22) follows from this simplification.  $M_{sc}$  can be interpreted as the mass flux in radiative-convective equilibrium. Mass continuity requires  $M_{sc} \approx M$ .

## 2.2. Theory 2: convection in a zero-buoyancy world

As first demonstrated by Singh & O’Gorman (2013), the vertical integral of cloud buoyancy taken relative to the clear-sky environment in convection-resolving model simulations is near zero. Based on this insight, they proposed a conceptual model of convection in which clouds are exactly neutrally-buoyant with respect to their environment. This assumption about typical cloud buoyancies is known as the *zero-buoyancy approximation*. Romps (2014, 2016) introduced an analytical model of zero-buoyancy convection, in which the steady-state humidity and temperature fields of the atmosphere are determined by the turbulent interaction between convective plumes and their environment.

The requirement that entraining clouds are neutrally buoyant with respect to the environment does not imply zero CAPE, which specifically depends on the buoyancy of a non-entraining parcel/plume relative to its environment. To see this, consider the formal definition of CAPE (Equation 1). Equations 1 and 12 tell us that two variables are required to estimate CAPE:  $\rho'$  and  $\rho$ . It is straightforward to calculate  $\rho'$  given surface boundary conditions. What is

<sup>5</sup> Equation 17 is typically utilized as a way of estimating CAPE (Rennó & Ingersoll 1996; Emanuel & Bister 1996).

<sup>6</sup> The tropospheric minimum in MSE tends to be near the net emission level, so one would obtain similar results using an air parcel at  $\overline{T}_A$  to represent the cloud layer instead.

<sup>7</sup> The intriguing possibility for lower-tropospheric radiative heating ( $Q_{A,sc} > 0$ ) to violate quasi-equilibrium could be explored in future work through Equations 19 and 22.



needed to find CAPE, therefore, is a plausible environmental profile of  $\rho$ . The environmental  $\rho$  is equal to the density of an *entraining* plume in the zero-buoyancy approximation, and this is what allows a closed-form model of CAPE. The zero-buoyancy model of CAPE has been validated against convection-resolving model simulations (Romps 2016; Seeley & Wordsworth 2023).

Below, we re-derive the zero-buoyancy theory of CAPE (Romps 2016) in order to estimate its dependence on surface temperature and moisture. We begin by approximating the saturation specific humidity as

$$q^* = \frac{R_a}{R_v} \frac{e^*}{p}, \quad (23)$$

where  $R_a$  is the specific gas constant of environmental air (everywhere assumed to be that of dry air) and  $p$  is the total air pressure. Taking the vertical derivative of the natural log of  $e^*$  (and using the definition of the lapse rate  $\Gamma = -\partial_z T$ ), we obtain

$$\begin{aligned} \partial_z e^* &= \partial_T e^* \partial_z T = -\frac{L e^* \Gamma}{R_v T^2}, \\ \partial_z \ln e^* &= -\frac{L \Gamma}{R_v T^2}. \end{aligned} \quad (24)$$

The vertical derivative of the natural log of  $p$  is obtained from hydrostatic balance and the ideal gas law:

$$\partial_z \ln p = -\frac{g}{R_a T}, \quad (25)$$

where  $g$  is gravity. Taking the vertical derivative of the natural log of  $q^*$  and plugging in Equations 24 and 25, we obtain

$$\begin{aligned} \partial_z \ln q^* &= \partial_z \ln e^* - \partial_z \ln p, \\ &= \frac{g}{R_a T} - \frac{L \Gamma}{R_v T^2} = -\gamma. \end{aligned} \quad (26)$$

where  $\gamma$  is the water vapor lapse rate ( $\text{kg kg}^{-1} \text{m}^{-1}$ ). The tropospheric water budget is obtained from the bulk-plume equations for convection in steady-state:

$$\partial_z M = e - d - c, \text{ where } e = \varepsilon M \text{ and } d = \delta M, \quad (27)$$

$$\partial_z (M q^*) = e q - d q^* - c, \text{ and} \quad (28)$$

$$-\partial_z (M q) = d q^* - e q + \alpha c. \quad (29)$$

$M$  is the convective mass flux ( $\text{kg m}^{-2} \text{s}^{-1}$ ),  $e$  and  $d$  are the turbulent entrainment and detrainment rates ( $\text{kg m}^{-3} \text{s}^{-1}$ ) in which  $\varepsilon$  and  $\delta$  are fractional mixing efficiencies ( $\text{m}^{-1}$ ), and  $c$  is the condensation rate ( $\text{kg m}^{-3} \text{s}^{-1}$ ).  $\alpha$  is defined as the ratio of gross evaporation to gross condensation at each height, so the gross evaporation is  $\alpha c/M$  and the condensation minus evaporation is  $\text{PE} c/M$ , where  $\text{PE} = (1 - \alpha)$  is the precipitation efficiency.<sup>8</sup> We make the following assumptions. The condensates not re-evaporated at each level ( $\text{PE} c/M$ ) are immediately removed from the convective plume. The gross condensation represents a small fraction of the total updraft mass ( $\partial_z M \gg c$ ). Invoking the latter assumption in Equation 27 gives

$$\begin{aligned} \partial_z M &= e - d \\ &= (\varepsilon - \delta) M. \end{aligned} \quad (30)$$

Expanding Equation 28 with the chain-rule and solving for  $\partial_z q^*$  (using Equation 30), we obtain

$$\partial_z q^* = \varepsilon (q - q^*) - \frac{c}{M}. \quad (31)$$

<sup>8</sup> Re-evaporation in the atmosphere constitutes an irreversible source of entropy (Emanuel 2001), which is neglected in the heat engine model (Emanuel & Bister 1996).



Doing the same to Equation 29 to find  $\partial_z q$ ,

$$-\partial_z q = \delta(q^* - q) + \alpha \frac{c}{M}. \quad (32)$$

The relative humidity is approximated as  $\text{RH} = q/q^*$ . Rearranging for  $q$ ,

$$q = \text{RH}q^*, \quad (33)$$

and taking the vertical derivative of both sides, we obtain

$$\partial_z q = q^* \partial_z \text{RH} + \text{RH} \partial_z q^*. \quad (34)$$

We assume that vertical variations in RH are much smaller than those in specific humidity ( $\partial_z \text{RH} \ll \partial_z q^*$ ), as is generally the case in Earth's troposphere. Invoking this assumption in Equation 34 gives

$$\partial_z q = \text{RH} \partial_z q^*. \quad (35)$$

Using Equations 26, 33, and 35 to re-write Equations 28 and 29, we obtain

$$-\gamma q^* = \varepsilon(\text{RH} - 1)q^* - \frac{c}{M} \quad \text{and} \quad (36)$$

$$\text{RH} \gamma q^* = \delta(1 - \text{RH})q^* + \alpha \frac{c}{M}. \quad (37)$$

To solve for RH, we substitute  $\frac{c}{M}$  from Equation 36 into Equation 37.

$$\text{RH} = \frac{\delta + \alpha \gamma - \alpha \varepsilon}{\delta + \gamma - \alpha \varepsilon} \quad (38)$$

We invoke the zero-buoyancy assumption (Singh & O’Gorman 2013) to define the MSE ( $h$ ) of the environment and the plume.

$$h = c_p T + gz + Lq \quad (39)$$

$$h^* = c_p T + gz + Lq^* \quad (40)$$

In the zero-buoyancy assumption, convective plumes are neutrally buoyant with respect to their environment. Strictly speaking, this means that their *virtual* temperatures are the same. When virtual effects are neglected, as is done here, the plume and the environment possess the same temperature  $T$  such that their moist static energies differ only by the differences in their specific humidities.  $c_p$  is the specific heat of the atmosphere (assumed to be dry air,  $c_{pa}$ ). Next, taking the vertical derivative of  $h^*$  (and using  $\Gamma = -\partial_z T$ ,  $\partial_z q^* = -\gamma q^*$ , and Equation 26),

$$\begin{aligned} \partial_z h^* &= -c_p \Gamma + g - L \gamma q^* \\ &= g \left( 1 + \frac{L q^*}{R_a T} \right) - \Gamma \left( c_p + \frac{L^2 q^*}{R_v T^2} \right). \end{aligned} \quad (41)$$

It follows from Equation 27 that the vertical change in MSE flux with height for an entraining plume is

$$\partial_z (M h^*) = (\varepsilon h - \delta h^*) M. \quad (42)$$

Using the chain rule to solve for  $\partial_z h^*$  (and substituting Equations 30, 39, and 40):

$$\begin{aligned} \partial_z h^* &= \varepsilon(h - h^*) \\ &= \varepsilon(q - q^*)L \\ &= \varepsilon(\text{RH} - 1)Lq^*. \end{aligned} \quad (43)$$

By convention (Romps 2016; Seeley & Wordsworth 2023), the “bulk-plume parameter” is defined:

$$a = \text{PE} \frac{\varepsilon}{\gamma}. \quad (44)$$

We will assume that  $M$ ,  $\text{RH}$ , and  $\alpha$  are all constant with height. Note that the assumption of constant  $M$  is used in both the zero-buoyancy model and the quasi-equilibrium heat engine model. By these assumptions,  $\varepsilon = \delta$  (Equation 30),  $\varepsilon \propto \gamma$  (Equation 38), and  $a$  is constant with height. Equation 44 can be re-arranged to solve for  $\varepsilon$ , while  $\text{RH}$  (Equation 38) simplifies to

$$\varepsilon = \frac{\gamma a}{\text{PE}} \text{ and} \quad (45)$$

$$\text{RH} = \frac{1 + a - \text{PE}}{1 + a}. \quad (46)$$

Substituting Equations 45 and 46 into Equation 43,

$$\partial_z h^* = -\frac{a}{1+a} \gamma L q^*. \quad (47)$$

Equating Equations 41 and 47 and solving for  $\Gamma$ ,

$$\Gamma = \frac{g}{c_p} \left[ \frac{1 + a + q^* L / (R_a T)}{1 + a + q^* L^2 / (c_p R_v T^2)} \right]. \quad (48)$$

Equation 48 is the temperature lapse rate set by entraining convection and is accurate when the water vapor mixing ratio is less than one. By neglecting virtual effects, the convective available potential energy (Equation 1) in steady-state becomes

$$\text{CAPE} \approx \int_{\text{LCL}}^{\text{LNB}} g \frac{T' - T}{T} dz, \quad (49)$$

where  $T'$  is the temperature of a pseudo-adiabatic parcel and  $T$  is the environmental temperature. We obtain  $T'$  and  $T$  by integrating the zero-buoyancy model vertically with  $a = 0$  and  $a \geq 0$ , respectively.  $\text{PE}$  and  $a$  are prescribed constants; by Equation 45, their ratio is a constant equal to  $\gamma/\varepsilon$  ( $\gamma$  and  $\varepsilon$  both increase with height but do so in lock-step). Given  $\text{PE}$  and  $a$ , a self-consistent solution for  $\text{RH}$  can be found (Equation 46).  $a$  controls the moist coupling between convective plumes and environmental air (for further discussion, see Seeley & Wordsworth 2023). For non-entraining convection ( $a = 0$ ),  $\Gamma$  equals the moist adiabatic lapse rate,  $\Gamma_m$ . As  $a$  increases, the tighter coupling between the plume and the environment forces  $\Gamma$  apart from  $\Gamma_m$  (Seeley & Wordsworth 2023), permitting more CAPE in steady-state.<sup>9</sup>

To summarize, the system of equations for a convecting atmosphere in radiative-convective equilibrium under the zero-buoyancy approximation are  $q$  and  $q^*$ ,  $\gamma$ ,  $\text{RH}$ ,  $\Gamma$ , and  $\text{CAPE}$ . The final forms of the equations assume that the convective mass flux, the relative humidity of the environment, and precipitation efficiency ( $\text{PE}$  - defined as the fraction of condensates generated in updrafts at each height that are not re-evaporated) are constant with height. The thermodynamic constants and their units and values in “Earth-like” and “Titan-like” conditions are given in Table 1 and are also assumed to be constant with height.

### 2.3. The equilibrium condition

Emanuel & Bister (1996) equate  $M$  (Equation 18) and  $M_{sc}$  (Equation 22) to derive an expression for  $\text{CAPE}$ . This is clearly necessary for statistical equilibrium, in which there is no net vertical transport of mass. Doing so, we find that QE convection requires a conversion of the vertical MSE difference ( $\Delta h$ ) into  $\text{CAPE}$  at an efficiency  $\eta$ :

$$M \approx M_{sc} \rightarrow \eta \Delta h \approx \text{CAPE}. \quad (50)$$

Henceforward, Equation 50 is called the *equilibrium condition*. To estimate  $\text{CAPE}$  and  $\Delta h$ , we instead use a zero-buoyancy model of convection (see Section 2.2). It’s important to note that the  $\text{CAPE}$  predicted by the zero-buoyancy model represents a steady-state storage of buoyancy, not the rate of  $\text{CAPE}$  generation and destruction by radiation and convection.

We pose the following question: Is there a regime where  $M$  and  $M_{sc}$  don’t equal one another, and if so, what does that imply about convection? In such a regime, QE convection would be incompatible with radiative-convective equilibrium.

<sup>9</sup> Note that  $\text{CAPE}$  is an explicit function of  $a$  (Equation 48), whereas its dependence on  $\text{PE}$  is implicit (Equation 44).

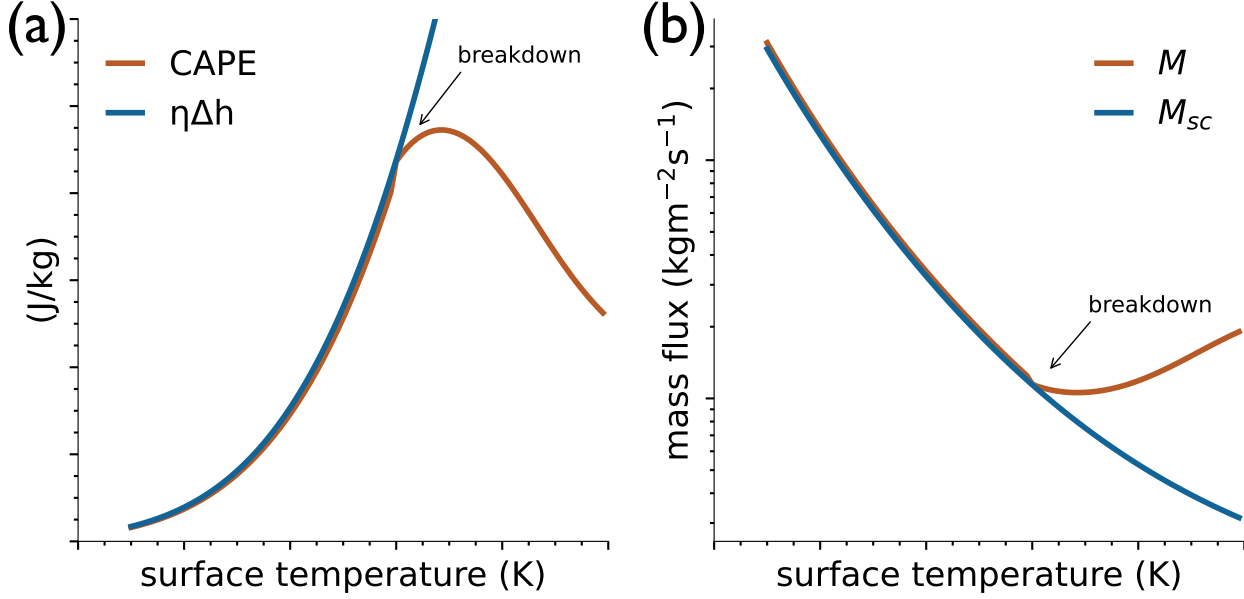


**Figure 3.** Schematic illustration of the breakdown of convective quasi-equilibrium with increasing temperature. (a) Comparison of convective available potential energy (CAPE;  $\text{Jkg}^{-1}$ ) and the vertical MSE difference ( $\Delta h$ ;  $\text{Jkg}^{-1}$ ) times the heat engine efficiency  $\eta$  as a function of surface temperature. (b) Comparison of the heat engine mass flux  $M \propto 1/\text{CAPE}$  and the subcloud mass flux  $M_{sc} \propto 1/\Delta h$  as a function of surface temperature. Quasi-equilibrium breaks down when  $\eta\Delta h > \text{CAPE}$ , as this indicates  $M > M_{sc}$ .

We argued previously that  $M \propto 1/\text{CAPE}$  (Equation 18) and  $M_{sc} \propto 1/\Delta h$  (Equation 22), so any constraint on mass fluxes naturally applies to CAPE and  $\Delta h$ . This is depicted schematically in Figure 3. Of course,  $\Delta h$  can increase without restriction (up to the limit of a steam atmosphere) as moisture increases by the Clausius-Clapeyron relation (Figure 3a). This implies that  $M_{sc}$  decreases monotonically (Figure 3b). However, convection in the zero-buoyancy model has a peak in CAPE at intermediate surface temperatures (Figure 3a; Seeley & Wordsworth 2023) due to the increasing influence of latent heat on the “effective” heat capacity of the troposphere (Romps 2016), implying a lower bound on  $M$  but no upper bound (Figure 3b). If  $M < M_{sc}$ , the heat engine of the cloud layer would be over-driven, this would likely reduce CAPE, and the system would adjust to QE. This adjustment process implies  $M \approx M_{sc}$  is a characteristic of QE, which is the condition invoked by others to constrain CAPE (Rennó & Ingersoll 1996; Emanuel & Bister 1996). Clearly, our theory also predicts  $M > M_{sc}$  at surface temperatures above the threshold where  $\eta\Delta h > \text{CAPE}$  (Figure 3b). In this case, the subcloud layer cannot meet the mass flux demand required of the cloud layer heat engine, the layers decouple, and the cloud is cut off from the moisture source – steady, QE convection cannot exist in this regime. Lacking convection, CAPE would build over time until  $M \approx M_{sc}$ , triggering convection. Our “QE-breakdown” hypothesis for the emergence of RO convection is simply:

$$\eta\Delta h > \text{CAPE}. \quad (51)$$

### 3. TESTING THE THEORY AGAINST CONVECTION-RESOLVING MODEL SIMULATIONS

We now test the zero-buoyancy heat engine theory of convection against convection-resolving model simulations from Seeley & Wordsworth (2021a). We use separate procedures to obtain estimates for  $\eta$ ,  $\Delta h$ , and CAPE from the theory and from the simulations, which are described below. Some elements of the theory must be diagnosed from the simulations, so by “testing” we mean that we are establishing consistency between QE breakdown of the heat engine model and the onset of the RO state in simulations.

To calculate the steady-state CAPE in the simulations as a function of surface temperature (Figure 4a), we use the standard formula that includes virtual effects (Equation 1). The temperature of the “adiabatic” parcel varies with height in accordance with the conservation of the sum of MSE and CAPE (i.e., MSE+CAPE; Romps 2015; Marquet 2016). We parameterize condensed water loss from the parcel as exponential decay over a length scale of 5 km following

Convection-resolving model simulations from Seeley and Wordsworth (2021)

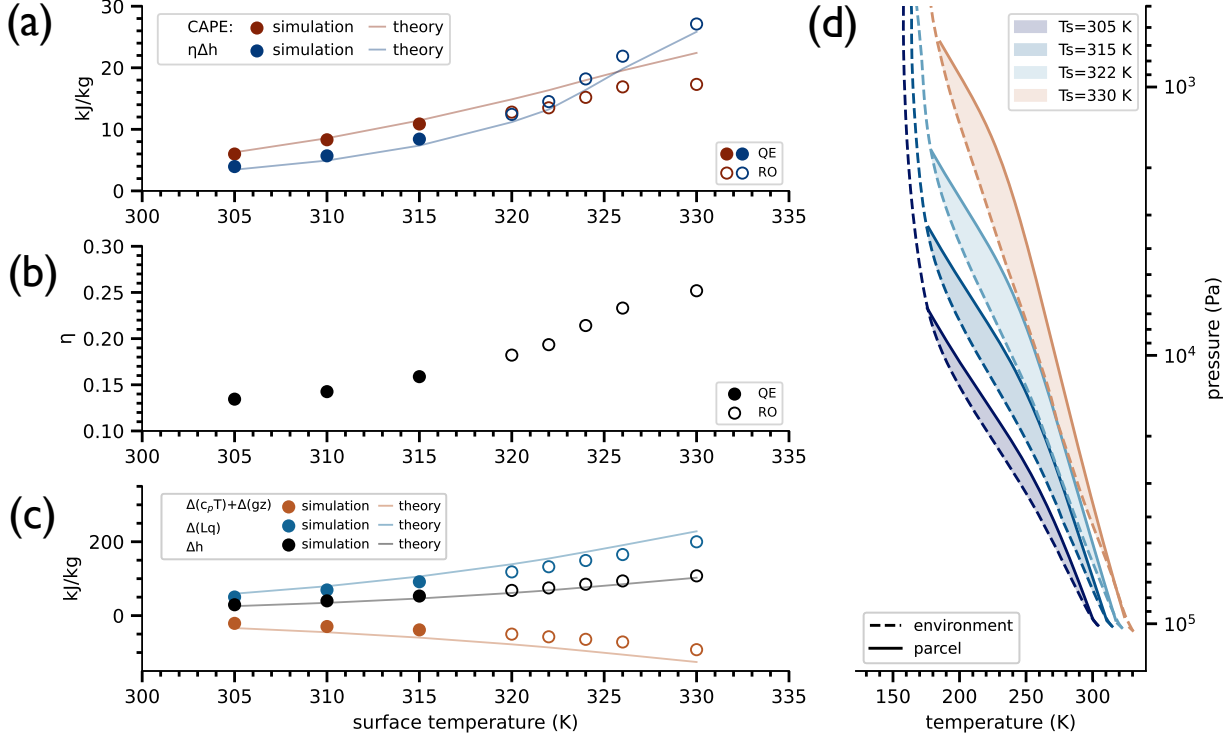


**Figure 4.** (a) Comparison of convective available potential energy (CAPE;  $\text{J kg}^{-1}$ ) and the vertical MSE difference ( $\Delta h$ ;  $\text{J kg}^{-1}$ ) times the heat engine efficiency  $\eta$  as a function of surface temperature. (b) Comparison of  $\eta$  (blue) with the maximum theoretical efficiency,  $\eta_{max}$  as a function of surface temperature. (c) Dry  $\Delta(c_p T)$  and moist  $\Delta(Lq)$  contribution to the MSE difference of upward and downward plumes across the LCL as a function of surface temperature. (d) Temperature difference of the environment and an adiabatically-lifted surface parcel. The magnitude of the shaded area is roughly proportional the steady-state CAPE in the simulation.

Seeley & Wordsworth (2023). The implementation of the MSE+CAPE parcel lifting method is detailed in Appendix C following Romps (2015).

To obtain a theoretical prediction for CAPE, we initialize the zero-buoyancy model with the temperature and pressure of a near-surface parcel at the LCL. The precipitation efficiency (PE) and the relative humidity (RH) as a mass-weighted tropospheric mean are determined from the simulation. We diagnose the precipitation efficiency as the ratio of the surface precipitation rate ( $P_s$ ;  $\text{kg m}^{-2} \text{s}^{-1}$ ) to the vertically-integrated sink of water vapor associated with phase changes (SI;  $\text{kg m}^{-2} \text{s}^{-1}$ ) following Sui et al. (2007):

$$\text{PE} = \frac{P_s}{\text{SI}}. \quad (52)$$

By substituting PE and RH into Equation 46, we obtain a self-consistent estimate for the bulk-plume parameter in the simulation:

$$a = \max\left(\frac{1 - \text{RH} - \text{PE}}{\text{RH} - 1}, 0\right). \quad (53)$$

$a$  quantifies the strength of the coupling between entraining plumes and their environment, taking into account both entrainment and re-evaporation. The constraint that  $a \geq 0$  follows from the requirement that  $\text{RH} \geq 1 - \text{PE}$  (Romps 2014). When  $a = 0$ ,  $\text{RH} = 1 - \text{PE}$  and environmental temperatures follow the moist adiabat. For those interested, Figure 7b-d in Appendix B shows PE, RH, and  $a$  from the convection-resolving model of Seeley & Wordsworth (2021a). Representative parameter values of the quasi-equilibrium state in the convection-resolving model ( $\text{RH} = 0.82$ ,

PE = 0.27, and  $a = 0.5$ ) are used to evaluate the zero-buoyancy model as a function of temperature. Figure 4a shows the theoretical and simulated CAPE. The simulated CAPE steadily increases in the convection-resolving model experiments of Seeley & Wordsworth (2021a) from 6 kJ/kg to 17 kJ/kg over the surface temperature range of 305-330 K. The growth in CAPE is explained by Figure 4d, which compares the environmental temperature to that of a surface parcel displaced adiabatically to the level of neutral buoyancy. CAPE is proportional to shaded area between the two curves in Figure 4d that represents the temperature difference between the environment and the parcel, where it can be seen that the size of the shaded area increases with surface warming.

The heat engine efficiency  $\eta$  (Equation 16) depends on the mean temperature at which turbulence is dissipated ( $\bar{T}_{irr}$ ) and the mean inverse temperatures at which radiation is absorbed at the surface ( $1/T_s$ ) and emitted from the atmosphere ( $1/\bar{T}_A$ ). The maximum efficiency of the convective heat engine ( $\eta_{max}$ ; Figure 4b) would be achieved if the dissipation of convective turbulence occurs only at the surface and the net emission level corresponds to the tropopause,  $\eta_{max} = (T_s - T_{trp})/T_{trp}$ , where  $T_{trp}$  is an assumed tropopause temperature of 200 K.  $T_s$  and  $T_{trp}$  clearly represent the warmest and coldest points of the system, respectively. Over the surveyed surface temperature range,  $\eta_{max}$  takes values between 52-65%. Rather than assuming the maximum efficiency, we make the reasonable assumption that most of the convective turbulence occurs between the surface and the effective emission level such that  $\bar{T}_{irr} = (T_s + \bar{T}_A)/2$ . Lacking a theory for the radiative cooling of the atmosphere,  $Q_A$  ( $\text{W kg}^{-1}$ ), we instead obtain it from the model output of Seeley & Wordsworth (2021a), which yields our estimate for  $\eta$  with realistic radiation (Figure 4b). We find that  $\bar{T}_A$  ranges from 258 K to 272 K (Figure 7a) in the simulations. Since the heat engine efficiency is sensitive to the radiation, we treat the simulation values as the “theoretical” prediction for  $\eta$ . The predicted efficiency is almost 15% at 305 K, and increases with surface warming up to 25% at 330 K. Raising the surface temperature drives more water vapor in the atmosphere, which increases radiative absorption at infrared and visible wavelengths. The spectral region over which the present-day atmosphere is transparent to infrared radiation (i.e., the water vapor window) begins to close at surface temperatures greater than 300 K, and becomes fully opaque at 320 K due to water vapor continuum absorption (Koll & Cronin 2018). Thus, the radiative properties of water vapor reduce  $\bar{T}_A$  with surface warming above 320 K (Figure 7a), which along with increasing surface temperatures further increases  $\eta$ .

The vertical difference in MSE,  $\Delta h$  (Equation 21), dry static energy,  $\Delta(c_p T) + \Delta(gz)$ , and latent energy,  $\Delta(Lq)$  are displayed in Figure 4c. Our method of evaluating  $\Delta h$  in the simulations and the theory is described in Section 2.1.1. There is no boundary layer in the zero-buoyancy model (Section 2.2), so we take the MSE of the sub-cloud layer to be that of the lowest atmospheric layer in the simulation. Then, we take the MSE of the cloud layer to be the MSE minimum in the zero-buoyancy model. The theoretical  $\Delta h$  slightly underestimates the simulated values, which increase from 29 kJ/kg to 107 kJ/kg over the experimental range of surface temperatures (Figure 4c). The steady growth in  $\Delta h$  reflects a competition between the increasing latent energy difference and the decreasing dry static energy difference. The vertical latent energy difference represented by  $\Delta(Lq)$  is dependent on temperature through the Clausius-Clapeyron relation, explaining its positive rise from 50 kJ/kg to 200 kJ/kg (Figure 4c). A larger and more negative vertical difference in dry static energy of -21 kJ/kg to -92 kJ/kg develops because of the expansion of the troposphere with surface warming. This expansion yields a larger geopotential energy difference in which  $\Delta(gz) < 0$ , and this cancels out the positive growth in  $\Delta(c_p T) > 0$  (not shown). Overall, the growth in  $\Delta h$  is fueled by latent component (Figure 4c).

The equilibrium condition implies that there should be a breakdown of steady, QE convection if  $\text{CAPE} < \eta \Delta h$ . In the simulations of Seeley & Wordsworth (2021a), we see that  $\text{CAPE} < \eta \Delta h$  above surfaces temperature of 320 K (circles in Figure 4a), which coincides with the transition into the RO regime. The zero-buoyancy heat engine theory (lines in Figure 4a) predicts the breakdown of QE convection within 5 K of the onset of RO convection, using QE values of the convective parameters from the simulation (Figure 7b-d). Their simulations show an increase in  $\eta \Delta h$  with surface warming largely due to the increase in  $\Delta(Lq)$ . Convection transports more energy per unit mass of cloudy air in warmer climates. The efficiency of the convective heat engine also increases in warmer climates partly due to the increase in surface temperatures and partly due to the radiative properties of water vapor, which shift the net emitting level upward. In summary, the convection-resolving simulations seem to support our zero-buoyancy heat engine hypothesis – RO convection emerges due to a breakdown in QE convection, which is caused by radiative and thermodynamic effects of increases in water vapor.

#### 4. RO STATES EXIST IN A SINGLE-COLUMN MODEL OF RADIATIVE-CONVECTIVE EQUILIBRIUM

We’ve demonstrated an important contradiction between quasi-equilibrium convection and radiative-convective equilibrium at high surface temperatures. This led us to a novel explanation for RO emergence. The heat engine (Section 2.1) and zero-buoyancy (Section 2.2) theories of convection posit only the existence of an ensemble of convective plumes that are in steady-state with their environment. The properties of the environment including temperature and relative humidity are determined by their mutual interaction with the cloud ensemble. While this conceptual model is based on three-dimensional reality (Figure 2), the assumption of horizontal homogeneity in temperature of the ZBM allows for the governing equations to be evaluated as a function of height alone. Indeed, the only consideration of horizontal variations is implicit in the humidity difference between entraining plumes and the environment. These plumes are not spatially resolved but instead their bulk properties are diagnosed from the large-scale environmental variables. Hydrostatic climate models parameterize convective processes in a single vertical dimension using this bulk-plume approach.

We see no a-priori reason why a single-column model of radiative-convective equilibrium should not exhibit RO dynamics at high surface temperatures so long as the convection scheme represents steady-state ascending and descending motion by such a bulk-plume parameterization. As in the case with resolved convection, we should expect RO dynamics in a single-column model of radiative-convective equilibrium if  $\text{CAPE} < \eta \Delta h$ . To test these ideas, we reproduce the basic experimental setup of Seeley & Wordsworth (2021a) in a single-column climate model with a bulk-plume parameterization of convection.

#### 4.1. Model and Methods

We use a version of the ECHAM6 general circulation model (Stevens et al. 2013) in single-column mode that has been modified to allow water vapor to comprise a significant fraction of the atmospheric mass (Popp et al. 2015). The single-column model is forced only by surface heating and radiative cooling (i.e., radiative-convective equilibrium) and has separate schemes for radiation, convection, clouds, and turbulent fluxes.

##### 4.1.1. Base experiment

In our base experiment, we run simulations over a temperature range from 290 K to 360 K. The insolation is set 10% higher than the present-day value and is temporally fixed (no diurnal or seasonal cycle). We set the column latitude to 38°N, where the globally-averaged insolation is the same as the local value. Clouds are the only source of time-varying planetary albedo. The atmosphere is composed *only* of nitrogen, oxygen, carbon dioxide, and water. The molar mixing ratio of carbon dioxide is set to 354 ppmv and is uniform with height. We use a time step of 60 seconds and run the simulations for approximately 200 years. The surface temperature of a 1 m mixed-layer ocean with an albedo of 0.07 is fixed at every time step through the use of an artificial surface heat sink.

##### 4.1.2. Thermodynamics

The version of ECHAM6 that we use accounts for the contribution of water vapor to the total pressure, density, and heat capacity of the atmosphere. The model uses an empirical formula for the saturation vapor pressure of water over liquid and ice, respectively:

$$e^*(\text{Pa}) = \exp \left( c_1/T + c_2 + 10^{-2}c_3T + 10^{-5}c_4T^2 + c_5 \ln(T) \right) \quad (54)$$

$$\text{where } c_1, c_2, c_3, c_4, c_5 = \begin{cases} -6024.5282, 29.32707, 1.0613868, -1.3198825, -0.49382577 & \text{if } T \leq 273.15 \text{ K} \\ -6096.9385, 21.2409642, -2.711193, 1.673952, 2.433502 & \text{if } T > 273.15 \text{ K} \end{cases}$$

The constants take different values depending on whether the temperature (in units of Kelvin) is above or below the triple point temperature.

##### 4.1.3. Radiation

Shortwave and longwave radiation is resolved into 14 and 16 spectral bands by the Rapid Radiative Transfer Model for General Circulation Models (RRTMG - Iacono et al. 2008). RRTMG uses the correlated-k method under the two-stream approximation, where each band is further sub-divided on the basis of the strength of molecular absorption features. This results in a spectrally-integrated radiative heating rate with 140 pseudo-wavelengths in the longwave and 112 pseudo-wavelengths in the shortwave (Giorgetta et al. 2013). By default, the radiation calculation is performed



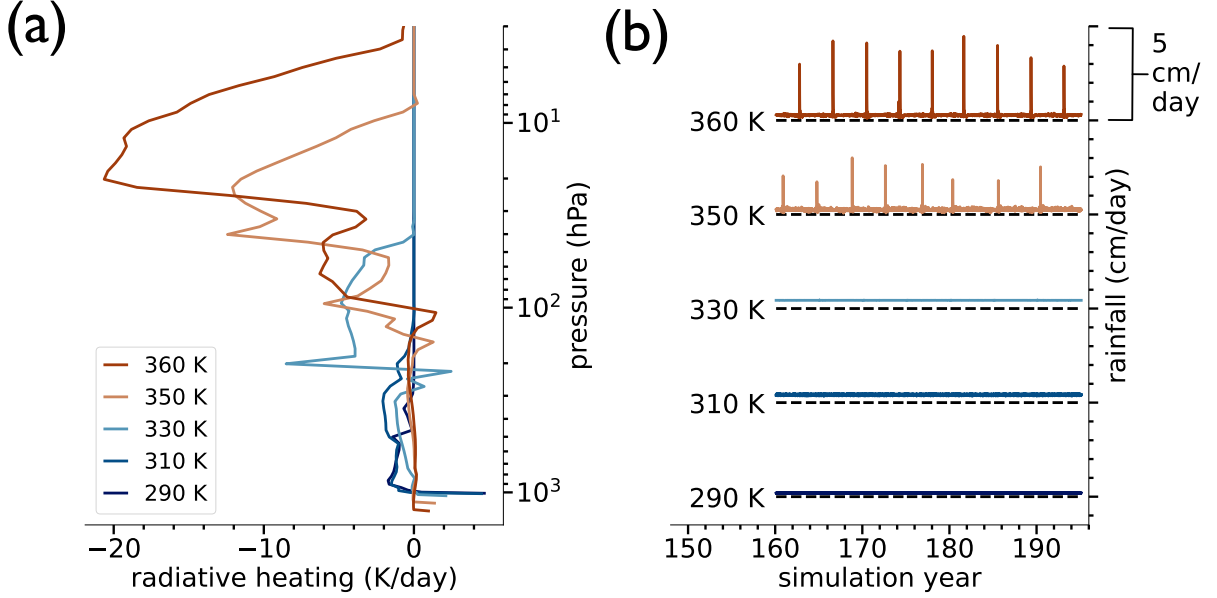


**Figure 5.** From the base experiment, (a) net radiative temperature tendency (K/day) and (b) time series of the surface precipitation rate (cm/day). Values in (a) are temporally-averaged over the multi-decadal period in (b). Time is given in years since the start of the simulation. Precipitation rates at each surface temperature are vertically offset by 5 cm/day and a zero rainfall contour is given for reference as a dashed black line.

once hourly. All forms of water besides precipitation are accounted for in the radiation calculation. As in [Popp et al. \(2015\)](#), we use an exponential extrapolation of all molecular absorption coefficients in the longwave and the water self-broadened absorption coefficients in the shortwave for temperatures above which no data in the original model exists. The effect of pressure broadening by water vapor is neglected.

#### 4.1.4. Convection

Convection is represented by the [Nordeng \(1994\)](#) bulk-plume scheme, which parameterizes turbulent entrainment and detrainment of air between updrafts, downdrafts, and the environment. The scheme distributes energy, moisture, and momentum through the column under the assumption that the cumulus ensemble is in steady-state. Downdrafts are initialized at the level of free sinking with the properties of a mixture of cloudy and saturated environmental air at their wet bulb temperature ([Giorgetta et al. 2013](#)). The level of free sinking is defined as the highest location where said mixture is negatively buoyant with respect to the environment. The downdrafts remain saturated by re-evaporating condensates produced by the convective updrafts. The initial downdraft mass flux is assumed to be directly proportional to the initial updraft mass flux ([Nordeng 1994](#)). Note that the zero-buoyancy model of [Romps \(2016\)](#) neglects condensate loading of updrafts (liquid water is instantly removed) and the effect of downdrafts associated with re-evaporation; it does, however, account for adiabatic subsidence in the environment (Section 2.2). For saturated updrafts undergoing pseudo-adiabatic ascent, the bulk-plume equations of [Nordeng \(1994\)](#) are the same as in the zero-buoyancy model of convection (Equations 28 and 30). The convection scheme has a quasi-equilibrium closure ([Neelin & Zeng 2000](#)) so that the cloud-base mass flux  $M_{cb} \propto \text{CAPE}/\tau$  where  $\tau = 2$  hours is an assumed adjustment time for CAPE ([Giorgetta et al. 2013](#)).<sup>10</sup> To ensure numerical stability, the permitted range of cloud base mass fluxes is  $10^{-10}$ – $1 \text{ kg m}^{-2}\text{s}^{-1}$  and convective temperature tendencies are limited to 0.05 K/s. We set the entrainment rate in the convection scheme to  $0.1 \text{ km}^{-1}$ , following [Popp et al. \(2015\)](#) and [Spaulding-Astudillo & Mitchell \(2023\)](#). The updraft mass flux is assumed to be constant up to a critical height set by the buoyancy of entraining convection, above which updrafts are only permitted to detrain ([Möbis & Stevens 2012](#)). The downdraft mass flux is assumed to be

<sup>10</sup> This closure to the cloud-base mass flux could conceivably produce large values of  $M_{cb}$  if, by some form of convective inhibition, significant CAPE is allowed to build up over a period of time before being released.



constant with height (Nordeng 1994; Tiedtke 1989). The trigger for shallow convection is based on the buoyancy of adiabatically lifted parcels relative to the environment at the cloud base (Möbis & Stevens 2012).

#### 4.1.5. Clouds

The large-scale cloud scheme has separate prognostic equations for the vapor, liquid, and ice phases of water, a modified microphysics scheme based on Lohmann & Roeckner (1996), and diagnostic cloud cover (Sundqvist et al. 1989). Sources and sinks of water from non-local transport processes such as convection and turbulence and local processes such as condensation, evaporation, deposition, sublimation, precipitation formation, re-evaporation of rain and sublimation of snow are included in the prognostic equations (Giorgetta et al. 2013). The amount of rain re-evaporation at each height is proportional to the local saturation deficit - that is, the difference between the saturation and environmental water vapor mixing ratio (Lohmann & Roeckner 1996). Cloud fraction is diagnosed at each time step as a function of the environmental relative humidity (Stevens et al. 2013). The cloud fraction is calculated only if the relative humidity is greater than a threshold value, which monotonically decreases with height. Condensational growth or evaporative decay of cloud droplets is conditional on whether the relative humidity is above or below this threshold (Giorgetta et al. 2013).

#### 4.1.6. Surface fluxes and eddy diffusion

Sensible and latent heat fluxes at the surface are determined by the standard bulk-exchange formulas. Vertical turbulent mixing is parameterized using the eddy-diffusivity approach of Brinkop & Roeckner (1995).

#### 4.1.7. Precipitation efficiency

We diagnose the precipitation efficiency in ECHAM6 in accordance with Equation 52, where

$$P_s = P_s^{ls} + P_s^u$$

and

$$SI = SI^{ls} + SI^u.$$

The superscripts “ls” and “u” refer to the large-scale environment and convective updrafts, respectively.  $P_s^{ls}$  and  $P_s^u$  are surface precipitation rates, which are determined separately by the large-scale cloud scheme and the convection scheme.<sup>11</sup>  $SI^{ls}$  and  $SI^u$  are the vertically-integrated gross sinks of water vapor associated with phase changes in the large-scale environment and in convective updrafts, respectively. The vertically-integrated gross sink of water vapor in the large-scale environment from the surface (SFC) to the tropopause (TRP) is

$$SI^{ls} = \int_{\text{SFC}}^{\text{TRP}} \left( \frac{\partial q}{\partial t} \right)^{ls} \frac{dp}{g},$$

where the gross large-scale sink of water vapor is

$$\left( \frac{\partial q}{\partial t} \right)^{ls} = \dot{q}_{cnd} + \dot{q}_{dep} + \dot{q}_{tbl} + \dot{q}_{tbi} < 0.$$

Here,  $\dot{q}_{cnd}$  and  $\dot{q}_{dep}$  are the condensation and deposition rates of water vapor, and  $\dot{q}_{tbl}$  and  $\dot{q}_{tbi}$  are the rates of cloud condensate generation (liquid and ice, respectively) through turbulent fluctuations (Giorgetta et al. 2013). The vertically-integrated sink of water vapor in convective updrafts from the cloud base (CB) to the cloud top (CT)

$$SI^u = - \int_{\text{CB}}^{\text{CT}} M_u \frac{\partial q_u}{\partial z} dz,$$

where  $M_u$  is the updraft mass flux and  $\frac{\partial q_u}{\partial z} < 0$  is the gross vertical change in updraft specific humidity due to condensation and/or deposition. This definition of  $SI^u$  excludes other processes that alter  $q_u$  with height but that are not associated with phase changes, such as entrainment. Downdrafts do not generate condensates in ECHAM6; the parameterized effect of downdrafts is to evaporate the condensates produced in updrafts in order to maintain their saturated descent, thereby reducing the overall convective precipitation.

<sup>11</sup> In a convection-resolving model, there is no distinction between  $P_s^{ls}$  and  $P_s^u$ .

## ECHAM6 single-column model simulations

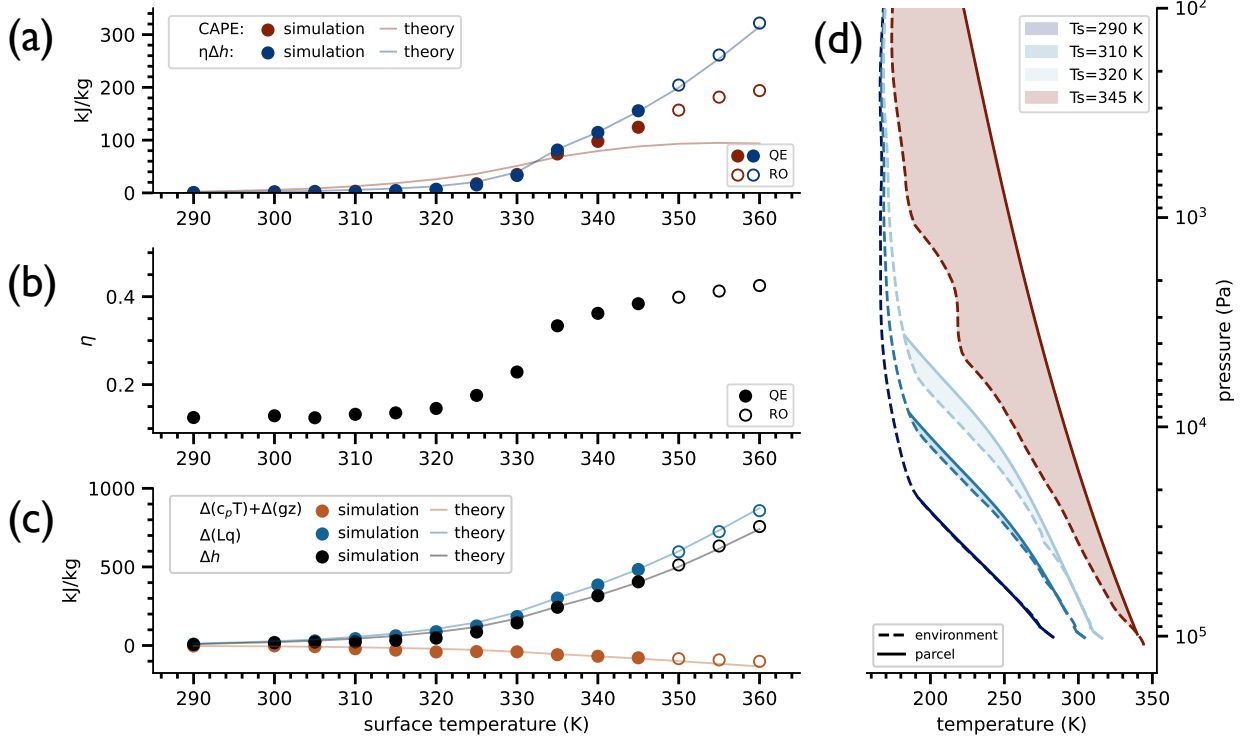


**Figure 6.** (a) Comparison of convective available potential energy (CAPE;  $\text{J kg}^{-1}$ ) and the vertical moist static energy difference ( $\Delta h$ ;  $\text{J kg}^{-1}$ ) times the heat engine efficiency  $\eta$  as a function of surface temperature. (b) Heat engine efficiency  $\eta$  as a function of surface temperature. (c) Dry  $\Delta(c_p T)$  and moist  $\Delta(Lq)$  contribution to the moist static energy difference of upward and downward plumes across the LCL as a function of surface temperature. (d) Temperature difference of the environment and an adiabatically-lifted surface parcel. The magnitude of the shaded area is roughly proportional the steady-state CAPE in the simulation.

#### 4.2. RO emergence is consistent with a breakdown of QE

To date, RO states have only been simulated in Earth models with resolved convection (Seeley & Wordsworth 2021a; Dagan et al. 2023; Song et al. 2023). Figure 5b clearly shows that the simulated climate in our base experiment transitions into the RO state at surface temperatures around 350 K. At cooler temperatures, precipitation is steady with a mean value of 2-6 mm/day; these simulations are in the QE regime. RO states exhibit episodic precipitation with intensities up to 5 cm/day that repeat every  $O(100 - 1000)$  days and that are relatively short-lived (10-30 days).<sup>12</sup> Here, we stress that the storm duration and frequency are inconsistent with previous estimates for hothouse climates. Convection-resolving models find that the storms last several hours and reappear in a matter of days (Seeley & Wordsworth 2021a; Dagan et al. 2023; Song et al. 2023). We speculate that these orders-of-magnitude differences arise from the parameterizations in our one-dimensional model. We cannot rule out the possibility that the driving physics of the RO regime are different between one-dimensional and three-dimensional models. Our partial replication of the RO regime in a single-column model underscores the important limitations of simpler parameterized climate models. The accuracy of the single-column model might be improved by tuning or overhauling existing parameterizations (see Appendix B), a task that we leave to future work.

Nonetheless, the existence of episodic precipitation in our one-dimensional simulations at high surface temperatures allows for a second test of the zero-buoyancy heat engine theory of convection. We determine the range of the convective parameters in the one-dimensional simulations over all surface temperatures to be  $0.4 \leq \text{PE} \leq 0.8$  (Figure

<sup>12</sup> The storm duration is calculated as the number of contiguous days where the precipitation rate is above the mean value.

7f),  $0.55 \leq \text{RH} \leq 0.95$  (Figure 7g), and  $0.3 \leq a \leq 7.9$  (Figure 7h). As in Section 3, we use PE and RH from the simulated QE states to diagnose an appropriate value for the bulk-plume parameter  $a$  in the single-column model, yielding PE = 0.62, RH = 0.81, and  $a = 2.33$  (Figure 7f-h).

CAPE,  $\eta$ , and  $\Delta h$  from the simulations are shown as multi-decadal averages in Figure 6, alongside their predicted values from the theory ( $\eta$  is exempt; see Section 3). The heat transport by convection as measured by the vertical MSE difference increases from 9 kJ/kg to 860 kJ/kg between 290 K and 360 K. The work done by convection as quantified by CAPE ranges from 17 J/kg at 290 K to 194 kJ/kg at 360 K (Figure 6a). The heat engine efficiency increases from  $\eta = 12\%$  to 42% over the experimental surface temperature range (Figure 6b). The zero-buoyancy model tends to capture the overall trend of CAPE and  $\Delta h$  in the simulations, though CAPE tends to be over-estimated and under-estimated at low and high surface temperatures, respectively. The theoretical fit to the simulated CAPE can be improved by relaxing the assumption of a single value for PE and  $a$  (not shown).

A comparative analysis of the metrics in the equilibrium condition yields several noteworthy findings. The first is that, while the theory reveals a peak in CAPE at intermediate surface temperatures (Seeley & Wordsworth 2023), we observe no clear peak in CAPE in the simulations because the environmental temperatures do not converge on the moist adiabat at high  $T_s$  (Figure 6d); this can be understood as the result of the model having a large value of  $a \sim 6$  (Figure 7h). The second finding is that quasi-equilibrium is violated ( $\text{CAPE} < \eta\Delta h$ ) at intermediate surface temperatures in both the theory and the simulations (approximately 335 K in both cases; Figure 6a). This behavior arises due to the dependence of CAPE,  $\Delta h$ , and  $\eta$  on atmospheric moisture concentration. Specifically, the growth rate of CAPE, unlike  $\Delta h$ , no longer conforms to the Clausius-Clapeyron rate at intermediate surface temperatures (Romps 2016; Seeley & Wordsworth 2023). CAPE is curtailed by its dependence on the tropospheric heat capacity, which is itself affected by the ballooning concentration of water vapor (Seeley & Romps 2015, 2016; Romps 2016). Meanwhile,  $\eta$  increases with surface warming (Figure 6b). Below 320 K, this increase is primarily due to warming the “hot” part of the system. Above 320 K, the radiative effects of water vapor cool the “cold” part of system (i.e., the net radiating level ascends; Figures 5a and 7e), which raises the efficiency as well. Third, RO-type precipitation is first observed in our simulations at 350 K (Figure 5b). At this surface temperature, quasi-equilibrium is clearly violated (Figure 6a). However, the emergence temperature is 15 K higher than would be predicted under the strictest theoretical interpretation of QE breakdown.<sup>13</sup> Despite the caveats, the one-dimensional simulations seem to support the idea that violating the equilibrium condition (Equation 50) leads to the emergence of RO convection.

## 5. DISCUSSION

There have been several past studies of hothouse climates on Earth with one-dimensional and three-dimensional models with parameterized convection (Wordsworth & Pierrehumbert 2013; Wolf & Toon 2015; Popp et al. 2015, 2016). All of these studies found low-level temperature inversions in hothouse climates despite different model assumptions, however none of them reported episodic precipitation. The models of Wolf & Toon (2015) and Popp et al. (2015, 2016) employ different parameterizations, but the common elements included prognostic water ice, liquid, and vapor (Rasch & Kristjánsson 1998; Lohmann & Roeckner 1996), a bulk-plume convection scheme with quasi-equilibrium closure (Zhang & McFarlane 1995; Nordeng 1994), two-stream radiative transfer using the correlated-k method (Wolf & Toon 2013; Iacono et al. 2008), parameterized ocean heat transport, and prognostic surface temperatures. In the three-dimensional studies, Wolf & Toon (2015) included a seasonal cycle with modern ocean-land surface configuration, whereas Popp et al. (2016) simulated a global aquaplanet with no seasonal cycle. Seeley & Wordsworth (2021a) were the first to report episodic precipitation in hothouse climates using a (regional) cloud-resolving model. For our single-column model simulations, we employed the same model as Popp et al. (2015, 2016) in single-column mode with parameterized convection, but we followed the experimental setup of Seeley & Wordsworth (2021a) with 10% higher insolation than present-day, a mixed-layer ocean, and fixed sea surface temperatures. Under these experimental conditions, the single-column model produces episodic precipitation at high surface temperatures.

It seems clear that relaxation-oscillator (RO) convection emerges in sufficiently warm and/or humid atmospheres. A novelty of this work is that RO convection is not only possible in convection-resolving, three-dimensional simulations (Seeley & Wordsworth 2021a; Dagan et al. 2023), but also in a single-column climate model with parameterized convection. That being said, the RO-type convection and precipitation that develops in our single-column simulations

<sup>13</sup> The online ECHAM6 calculation for CAPE uses buoyancy and lapse rate formulations that are behind the state-of-the-art (e.g., Appendix C), which could also influence our offline interpretation of the single-column model results.

does not closely resemble the characteristics of RO convection in three-dimensional convection-resolving simulations (Seeley & Wordsworth 2021a), which we address below.

A second novelty of this work is the development of an even simpler model for the emergence of RO convection; we hypothesized that RO convection emerges in warm/humid climates due to a breakdown of QE convection, and developed a predictive theory based a heat engine model for convection. In QE, the rate of atmospheric radiative cooling can be related to a rate of work (Equation 17), which is proportional to the mass flux and CAPE. In sufficiently warm and humid atmospheres, the steady-state storage of CAPE is curtailed (Seeley & Wordsworth 2023) as heating goes to the latent reservoir instead of increasing temperature and buoyancy (Romps 2016). The change in CAPE with surface warming can be calculated using an analytical theory of convection in which entraining plumes are neutrally buoyant with respect to their environment (Romps 2016), as cloudy regions are observed to be in Earth’s tropics (Singh & O’Gorman 2013). Holding radiative cooling fixed, QE demands that the convective mass flux *increase* with decreasing CAPE (Equation 18), as must occur at high temperatures where CAPE is decreasing. However, because the mass and energy budget of the convection must close in the sub-cloud layer, radiative cooling aloft is counterbalanced by convective heat transport, i.e. the MSE flux across the LCL. It’s intuitive that the MSE flux can grow rapidly as the surface temperature increases due to the exponential increase in saturation vapor pressure. Again holding radiative cooling fixed, this implies the sub-cloud mass flux must *decrease* with increasing surface temperatures (Equation 22). If the sub-cloud layer cannot supply the cloud layer with enough mass flux, there can be no QE state – an inevitable consequence of the growing disparity between the increase in energy of the sub-cloud layer and a slower increase and/or decrease in CAPE. This follows from the equilibrium condition (Equation 50) of a convective heat engine (Emanuel & Bister 1996), which requires (i) a statistical equivalence between vertical heat transport ( $M_{sc} \times \Delta h$ ; Equation 22) and radiative cooling ( $\bar{Q}_A$ ) and (ii) the conversion of said cooling into work ( $M \times \text{CAPE}$ ; Equation 49) at a thermodynamic efficiency ( $\eta$ ; Equation 16).

In addition to our theoretical arguments, we presented evidence from simulations with and without resolved convection in support of the idea that the RO mode of convection is preferred in conditions that violate the equilibrium condition. We emphasize that our analysis does not rule out the lower-tropospheric radiative heating hypothesis of Seeley & Wordsworth (2021a) as an explanation for RO emergence; future work should compare these differing perspectives. Our analysis was first performed on convection-resolving model data from Seeley & Wordsworth (2021a). We found that the equilibrium condition is violated around 320 K, which is consistent with the temperature of RO emergence in their simulations. We repeated the analysis on data from our one-dimensional model and found that  $\eta\Delta h$  first exceeds CAPE around 335 K, but that episodic precipitation emerges closer to 350 K. The RO state clearly emerges in conditions that violate QE, but the accuracy of the theoretical prediction is worse when applied to the single-column model. The heat engine perspective of convection suggests that the conditions that make the QE state energetically unsustainable – in this case, curtailed growth in CAPE and sustained increases in atmospheric heat transport and opacity with surface warming – causes the RO state to emerge. It is possible to obtain episodic convection in a one-dimensional climate model because modern parameterizations are able to represent the necessary physics in a single vertical dimension. This possibility is underscored by our usage of the bulk-plume equations of convection in the zero-buoyancy heat engine theory, which are, in turn, a simplified version of the Nordeng (1994) convection scheme in our one-dimensional climate model (Section 4.1). The existence of the QE-to-RO convective regime transition across the modeling hierarchy<sup>14</sup> explored here lends confidence to the robustness of this transition, and we have demonstrated that important insights can be gained from the simpler end of the modeling hierarchy.

Through the steady-state and energy balance assumptions, the theory tells us when steady convection *must* break down, but not necessarily *how* it happens. This limitation is intrinsic to equilibrium models, where there are no net forces. While it is reasonable to infer that steady convection ceases where quasi-equilibrium is incompatible with radiative-convective equilibrium, these constraints do not give insight into the physical forces acting on convective plumes at the QE-to-RO transition. Consequently, a common approach for determining why RO convection happens is to look for changes in atmospheric stability over time. In the non-equilibrium perspective, the presence of stable layers inhibits convection by reducing the buoyancy force acting on plumes or delaying convective triggering. There are several studies that have considered the effects of water vapor on inhibition (Li & Ingersoll 2015; Seeley & Wordsworth 2021a). For example, water vapor plays an important role in modulating convective activity in Saturn’s atmosphere.

<sup>14</sup> Our usage of the term “model hierarchy” differs from the conventional definition, which refers to an tiered system of models with each subsequent tier operating at a higher level of complexity.

The high molecular weight of water vapor compared to the non-condensing background gases suppresses convection until the slow cooling of the atmosphere makes it unstable. This mechanism has been put forward as an explanation for the intermittent, giant storms on Saturn (Li & Ingersoll 2015). In addition, the LTRH that is induced by water vapor in Earth’s hothouse climates is important for generating very stable layers, including near-surface temperature inversions (Wordsworth & Pierrehumbert 2013; Wolf & Toon 2015; Popp et al. 2015). These inversions cap the boundary layer, decoupling it from the overlying atmosphere, and are slowly eroded by re-evaporation processes associated with descending virga. Seeley & Wordsworth (2021a) demonstrated that increasing LTRH can tip the climate into the RO state. We speculate that this is also due to a breakdown of QE because LTRH likely increases  $\eta$  by changing the effective absorbing and emitting temperatures, and reduces CAPE and/or introduces convective inhibition. We leave it to future work to test this.

In our derivation of the zero-buoyancy heat engine model, we made a few notable assumptions, approximations, and omissions that introduce errors in the limit of a moisture-dominated atmosphere. Revisiting these assumptions is a necessary next step, but is beyond the scope of this paper. First, we assumed that a statistical balance exists between sources and sinks of entropy in Earth’s climate system (Equation 3), and furthermore that the dominant source is frictional dissipation and that the dominant sink is absorption and emission of radiation. This yields a unique relationship between radiative and convective processes (Singh & O’Neill 2022) and a prediction for the temperature of RO emergence. A simple balance between these processes is an excellent approximation in numerical simulations of dry convection (Pauluis & Held 2002a), but may not hold for moist convection. Several numerical studies claim that moist processes such as irreversible mixing of dry air and water vapor, re-evaporation, and rain sedimentation could be the dominant sources of entropy generation in Earth’s current atmosphere (Pauluis & Held 2002a,b; Romps 2008; Singh & O’Neill 2022). This calls into question the validity of our simplified entropy budget in warm and humid atmospheres. Unfortunately, the relative importance of dry vs. moist processes in the entropy budget has yet to be constrained by theory or simulation over a broad range of temperatures and humidities. To improve our prediction of RO emergence, one could include these additional processes in the entropy budget and repeat our analysis. Second, we neglected the effect of downdrafts, which contribute to the net buoyancy flux in real atmospheres. Their contribution to the entropy budget should also be considered. Third, we made an important omission in the zero-buoyancy theory of convection: the virtual effect of water vapor. The virtual effect impacts the magnitude of CAPE, particularly in water-rich atmospheres. Further exploration of these limitations is left to future work.

Our single-column model fails on important benchmarks set by convection-resolving models (Seeley & Wordsworth 2021a; Dagan et al. 2023). First, the latter models agree that RO states on Earth should have a storm duration of several hours with an intervening period of several days. Our model produces storms with a duration of a few weeks that reoccur every few years. This could be related to the high PE of the single-column model simulations (Figure 7f), which we suspect is related to the non-zero precipitation during calm intervals in Figure 5b; the convection scheme seems to have a minimum threshold for precipitation whether or not it would re-evaporate in lower layers due to a built-in assumption that there is no environmental re-evaporation of condensates above the base of the convective updrafts (see Appendix B). The model also produces very high values of CAPE, which can be understood by the large value of the inferred bulk plume parameter  $a$  that prevents the environment from becoming moist adiabatic. Second, our model transitions into the RO state at temperatures above 350 K, which is 30 K higher than in convection-resolving model simulations (Seeley & Wordsworth 2021a; Dagan et al. 2023; Song et al. 2023). This could be due to the large values of CAPE of the single-column model, which again is due to the large value of  $a$ ; Figure 3a demonstrates that increasing CAPE values drives the QE breakdown to higher temperatures. See Appendix B for more details. The performance of the single-column model depends on the parameterizations and the assumptions made in developing them. These simple models are typically tuned to the modern climate of the planet they are meant to represent, and therefore are not guaranteed to represent reality in extreme scenarios. If the RO states in our single-column model are indeed driven by the same physics as in a convection-resolving model, then it is clear that our model suffers from reduced realism, and we suspect the convective parameterization is to blame. It’s conceivable that with some additional tuning, the single-column model could improve relative to the cloud-resolving models, but this is beyond the scope of this work.

## 6. IMPLICATIONS FOR TITAN

While present-day Earth does not exhibit RO behavior (Figure 1a), it is clear that episodic storms of potentially great magnitude occur on present-day Titan (Schneider et al. 2012; Turtle et al. 2011; Faulk et al. 2017; Rafkin et al.



2022; Charnay et al. 2015; Mitchell & Lora 2016). Global simulations of Titan with realistic land surface hydrology by Faulk et al. (2020) with the Titan Atmospheric Model (Lora et al. 2015) depicted in Figure 1b resemble the one-dimensional (Figure 5d) and three-dimensional (Figure 1c; Seeley & Wordsworth 2021a) simulated RO states on Earth, where brief periods of intense rainfall give way to extended periods of little to no rain.

The alignment of the climate of Titan and the hothouse Earth clearly merits further study. One example of this alignment is their total precipitable moisture: that is, the depth of liquid that would one would obtain by condensing out all atmospheric moisture into a uniform layer at the surface. Titan’s atmosphere stores around 5 m of precipitable methane (Tokano et al. 2006). Though the globally-averaged surface temperature on Earth is nearly 200 K warmer, the total precipitable moisture in Earth’s atmosphere - just a few centimeters of water - is smaller because water on Earth has a volatility<sup>15</sup> ten times less than methane on Titan (Griffith et al. 2008; Spaulding-Astudillo & Mitchell 2023). A consequence of the high temperatures in the hothouse climate is that the total precipitable water rises above 0.5 m by 330 K (Seeley & Wordsworth 2021b), or to within an order of magnitude of the precipitable methane in Titan’s atmosphere, which has important implications for moist convection.

Titan represents a unique laboratory for further testing of the zero-buoyancy heat engine theory of convection. To illustrate this, we carry out a back-of-the-envelope calculation of the equilibrium condition for Titan. The only direct measurement of CAPE in Titan’s atmosphere comes from the Huygens probe, which landed at 10°S where the near-surface relative humidity was  $\sim 50\%$  (Mitchell & Lora 2016). Estimates of CAPE at the time and location of the Huygen’s probe descent vary, with values of 960 J/kg (Tokano et al. 2006), 60 J/kg (Barth & Rafkin 2007), and 120 J/kg (Griffith et al. 2008) reported. The disparity in these values supposedly stems from different formulations of the adiabatic lapse rate (Griffith et al. 2008). To the best of our knowledge, no direct estimation of the MSE profile at the Huygens landing site exists. Therefore, we rely on spatially- and temporally-averaged vertical MSE difference from Titan Atmospheric Model simulations (Figure 1b; Faulk et al. 2020), yielding  $\Delta h \approx 2500$  J/kg. MSE is well-mixed in the boundary layer and decreases with height from 5 km to 15 km, where the MSE minimum occurs (not shown). Assuming that  $\text{CAPE} \sim 100$  J/kg and  $\Delta h \sim 2500$  J/kg are representative of Titan’s modern climate, then  $\text{CAPE} < \eta \Delta h$  only if  $4\% \leq \eta \leq 31\%$ , where the theoretical upper limit for  $\eta$  assumes a tropopause (emitting) temperature of 71.5 K and a surface temperature of 94 K (Lindal et al. 1983). Coincidentally,  $4\% \leq \eta \leq 31\%$  is similar to the range of efficiencies in convection-resolving simulations of Earth (Figure 4b). However, if typical values of CAPE are instead  $\sim 1000$  J/kg on Titan, then  $\eta$  would have to exceed the maximum theoretical efficiency in order to facilitate a breakdown of QE convection, indicating that Titan’s episodic precipitation requires an alternative explanation.

An interesting question for future work is whether the dynamical similarity of Titan and the hothouse Earth can be linked to the breakdown of QE convection in both cases. The conceptual framework that we’ve proposed offers a robust point of comparison between planetary atmospheres based on the first and second laws of thermodynamics, which are system invariant. The theory is, moreover, agnostic of the composition of the working fluid and thus seems a promising framework to explain the dynamical similarity between Titan and the hothouse Earth. The theory could be extended to any planetary atmosphere with a condensing component and, because of this, it will find wide application in the solar system and beyond.

## ACKNOWLEDGEMENTS

This work was supported by NSF Grant 1912673 and an Early-Career Fellowship from the Center for Diverse Leadership in Science at UCLA. The authors thank Jake Seeley, Bowen Fan, and Namrah Habib for helpful discussions, Robin Wordsworth and an anonymous reviewer for valuable comments on an early draft of this manuscript, and Jake Seeley for recommending the use of a root finder in our adiabat solver. The authors have no conflicts of interest to declare. The data from this study (Spaulding-Astudillo & Mitchell 2024) is available at <https://doi.org/10.5281/zenodo.10982231>.

## REFERENCES

Arakawa, A., & Schubert, W. H. 1974, *Journal of Atmospheric Sciences*, 31, 674.

<sup>15</sup> Volatility is here defined as the saturation vapor pressure of a condensable at the typical temperature of the planetary surface.  
doi: [https://doi.org/10.1175/1520-0469\(1974\)031\(0674:IOACCE\)2.0.CO;2](https://doi.org/10.1175/1520-0469(1974)031(0674:IOACCE)2.0.CO;2)

Barth, E. L., & Rafkin, S. C. R. 2007, *Geophysical Research Letters*, 34, doi: <https://doi.org/10.1029/2006GL028652>

- Battalio, J. M., Lora, J. M., Rafkin, S., & Soto, A. 2022, *Icarus*, 373, 114623, doi: [10.1016/j.icarus.2021.114623](https://doi.org/10.1016/j.icarus.2021.114623)
- Brinkop, S., & Roeckner, E. 1995, *Tellus A*, 47, 197, doi: <https://doi.org/10.1034/j.1600-0870.1995.t01-1-00004.x>
- Charnay, B., Barth, E., Rafkin, S., et al. 2015, *Nature Geoscience*, 8, 362, doi: [10.1038/ngeo2406](https://doi.org/10.1038/ngeo2406)
- Chen, D., Dai, A., & Hall, A. 2021, *Journal of Geophysical Research: Atmospheres*, 126, e2020JD034198, doi: <https://doi.org/10.1029/2020JD034198>
- Dagan, G., Seeley, J. T., & Steiger, N. 2023, *Journal of Advances in Modeling Earth Systems*, 15, e2023MS003765, doi: <https://doi.org/10.1029/2023MS003765>
- Dhingra, R. D., Barnes, J. W., Brown, R. H., et al. 2019, *Geophysical Research Letters*, 46, 1205, doi: <https://doi.org/10.1029/2018GL080943>
- Emanuel, K. 2001, *International Geophysics*, 70, 225, doi: [10.1016/S0074-6142\(00\)80056-X](https://doi.org/10.1016/S0074-6142(00)80056-X)
- Emanuel, K. A. 1986, *Journal of Atmospheric Sciences*, 43, 585, doi: [https://doi.org/10.1175/1520-0469\(1986\)043<0585:AASITF>2.0.CO;2](https://doi.org/10.1175/1520-0469(1986)043<0585:AASITF>2.0.CO;2)
- . 1994, *Atmospheric convection* / Kerry A. Emanuel. (New York: Oxford University Press)
- Emanuel, K. A., & Bister, M. 1996, *Journal of Atmospheric Sciences*, 53, 3276, doi: [https://doi.org/10.1175/1520-0469\(1996\)053<3276:MCVABS>2.0.CO;2](https://doi.org/10.1175/1520-0469(1996)053<3276:MCVABS>2.0.CO;2)
- Faulk, S. P., Lora, J. M., Mitchell, J. L., & Milly, P. C. D. 2020, *Nature Astronomy*, 4, 390, doi: [10.1038/s41550-019-0963-0](https://doi.org/10.1038/s41550-019-0963-0)
- Faulk, S. P., Mitchell, J. L., Moon, S., & Lora, J. M. 2017, *Nature Geoscience*, 10, 827, doi: [10.1038/ngeo3043](https://doi.org/10.1038/ngeo3043)
- Giorgetta, M., Roeckner, E., Mauritsen, T., & Rast, S. 2013, *Berichte zur Erdsystemforschung* / Max-Planck-Institut für Meteorologie, 135
- Griffith, C. A., McKay, C. P., & Ferri, F. 2008, *The Astrophysical Journal*, 687, L41, doi: [10.1086/593117](https://doi.org/10.1086/593117)
- Griffith, C. A., Owen, T., Geballe, T. R., Rayner, J., & Rannou, P. 2003, *Science*, 300, 628, doi: [10.1126/science.1081897](https://doi.org/10.1126/science.1081897)
- Griffith, C. A., Owen, T., Miller, G. A., & Geballe, T. 1998, *Nature*, 395, 575, doi: <https://doi.org/10.1038/26920>
- Hörst, S. M. 2017, *Journal of Geophysical Research: Planets*, 122, 432, doi: <https://doi.org/10.1002/2016JE005240>
- Iacono, M. J., Delamere, J. S., Mlawer, E. J., et al. 2008, *Journal of Geophysical Research: Atmospheres*, 113, doi: [10.1029/2008JD009944](https://doi.org/10.1029/2008JD009944)
- Koll, D. D. B., & Cronin, T. W. 2018, *Proceedings of the National Academy of Sciences*, 115, 10293, doi: [10.1073/pnas.1809868115](https://doi.org/10.1073/pnas.1809868115)
- Lewis-Merrill, R. A., Moon, S., Mitchell, J. L., & Lora, J. M. 2022, *The Planetary Science Journal*, 3, 223, doi: [10.3847/PSJ/ac8d09](https://doi.org/10.3847/PSJ/ac8d09)
- Li, C., & Ingersoll, A. P. 2015, *Nature Geoscience*, 8, 398, doi: [10.1038/ngeo2405](https://doi.org/10.1038/ngeo2405)
- Lindal, G., Wood, G., Hotz, H., et al. 1983, *Icarus*, 53, 348, doi: [https://doi.org/10.1016/0019-1035\(83\)90155-0](https://doi.org/10.1016/0019-1035(83)90155-0)
- Lohmann, U., & Roeckner, E. 1996, *Climate Dynamics*, 12, 557, doi: [10.1007/BF00207939](https://doi.org/10.1007/BF00207939)
- Lora, J. M., Lunine, J. I., & Russell, J. L. 2015, *Icarus*, 250, 516, doi: [10.1016/j.icarus.2014.12.030](https://doi.org/10.1016/j.icarus.2014.12.030)
- Marquet, P. 2016, *Journal of the Atmospheric Sciences*, 73, 2565, doi: [10.1175/JAS-D-15-0299.1](https://doi.org/10.1175/JAS-D-15-0299.1)
- Mitchell, J. L., & Lora, J. M. 2016, *Annual Review of Earth and Planetary Sciences*, 44, 353, doi: [10.1146/annurev-earth-060115-012428](https://doi.org/10.1146/annurev-earth-060115-012428)
- Möbis, B., & Stevens, B. 2012, *Journal of Advances in Modeling Earth Systems*, 4, 1, doi: [10.1029/2012MS000199](https://doi.org/10.1029/2012MS000199)
- Neelin, J. D., & Zeng, N. 2000, *Journal of the Atmospheric Sciences*, 57, 1741, doi: [https://doi.org/10.1175/1520-0469\(2000\)057<1741:AQETCM>2.0.CO;2](https://doi.org/10.1175/1520-0469(2000)057<1741:AQETCM>2.0.CO;2)
- Nordeng, E. T. 1994, *Research Department Technical Memorandum*, 206, 1
- Pauluis, O., & Held, I. M. 2002a, *Journal of the Atmospheric Sciences*, 59, 125, doi: [https://doi.org/10.1175/1520-0469\(2002\)059<0125:EBOAAI>2.0.CO;2](https://doi.org/10.1175/1520-0469(2002)059<0125:EBOAAI>2.0.CO;2)
- . 2002b, *Journal of the Atmospheric Sciences*, 59, 140, doi: [https://doi.org/10.1175/1520-0469\(2002\)059<0140:EBOAAI>2.0.CO;2](https://doi.org/10.1175/1520-0469(2002)059<0140:EBOAAI>2.0.CO;2)
- Perron, J. T., Lamb, M. P., Koven, C. D., et al. 2006, *Journal of Geophysical Research: Planets*, 111, doi: <https://doi.org/10.1029/2005JE002602>
- Pierrehumbert, R. T. 2010, *Principles of Planetary Climate* (Cambridge University Press), doi: [10.1017/CBO9780511780783](https://doi.org/10.1017/CBO9780511780783)
- Popp, M., Schmidt, H., & Marotzke, J. 2015, *Journal of the Atmospheric Sciences*, 72, 452, doi: [10.1175/JAS-D-13-047.1](https://doi.org/10.1175/JAS-D-13-047.1)
- . 2016, *Nature Communications*, 7, 10627, doi: [10.1038/ncomms10627](https://doi.org/10.1038/ncomms10627)
- Rafkin, S. C., Lora, J. M., Soto, A., & Battalio, J. M. 2022, *Icarus*, 373, 114755, doi: [10.1016/j.icarus.2021.114755](https://doi.org/10.1016/j.icarus.2021.114755)



- Rasch, P. J., & Kristjánsson, J. E. 1998, *Journal of Climate*, 11, 1587 ,  
doi: [https://doi.org/10.1175/1520-0442\(1998\)011<1587:ACOTCM>2.0.CO;2](https://doi.org/10.1175/1520-0442(1998)011<1587:ACOTCM>2.0.CO;2)
- Rennó, N. O., & Ingersoll, A. P. 1996, *Journal of Atmospheric Sciences*, 53, 572 ,  
doi: [https://doi.org/10.1175/1520-0469\(1996\)053<0572:NCAAHE>2.0.CO;2](https://doi.org/10.1175/1520-0469(1996)053<0572:NCAAHE>2.0.CO;2)
- Romps, D. M. 2008, *Journal of the Atmospheric Sciences*, 65, 3779 , doi: [10.1175/2008JAS2679.1](https://doi.org/10.1175/2008JAS2679.1)
- . 2014, *Journal of Climate*, 27, 7432,  
doi: [10.1175/JCLI-D-14-00255.1](https://doi.org/10.1175/JCLI-D-14-00255.1)
- . 2015, *Journal of the Atmospheric Sciences*, 72, 3639 ,  
doi: [10.1175/JAS-D-15-0054.1](https://doi.org/10.1175/JAS-D-15-0054.1)
- . 2016, *Journal of the Atmospheric Sciences*, 73, 3719 ,  
doi: [10.1175/JAS-D-15-0327.1](https://doi.org/10.1175/JAS-D-15-0327.1)
- Romps, D. M., Charn, A. B., Holworth, R. H., et al. 2018, *Geophysical Research Letters*, 45, 12,623,  
doi: <https://doi.org/10.1029/2018GL080267>
- Schaller, E. L., Roe, H. G., Schneider, T., & Brown, M. E. 2009, *Nature*, 460, 873, doi: [10.1038/nature08193](https://doi.org/10.1038/nature08193)
- Schneider, T., Graves, S. D. B., Schaller, E. L., & Brown, M. E. 2012, *Nature*, 481, 58, doi: [10.1038/nature10666](https://doi.org/10.1038/nature10666)
- Seeley, J. T., & Romps, D. M. 2015, *Geophysical Research Letters*, 42, 10,429,  
doi: <https://doi.org/10.1002/2015GL066199>
- . 2016, *Geophysical Research Letters*, 43, 3572,  
doi: <https://doi.org/10.1002/2016GL068583>
- Seeley, J. T., & Wordsworth, R. D. 2021a, *Nature*, 599, 74,  
doi: [10.1038/s41586-021-03919-z](https://doi.org/10.1038/s41586-021-03919-z)
- . 2021b, Data and code for Seeley and Wordsworth (2021), "Episodic deluges in simulated hothouse climates", Zenodo, doi: [10.5281/zenodo.5636455](https://doi.org/10.5281/zenodo.5636455)
- . 2023, *The Planetary Science Journal*, 4, 34,  
doi: [10.3847/PSJ/acb0cb](https://doi.org/10.3847/PSJ/acb0cb)
- Seidel, S. D., & Yang, D. 2020, *Science Advances*, 6, eaba1951, doi: [10.1126/sciadv.aba1951](https://doi.org/10.1126/sciadv.aba1951)
- Singh, M. S., & O’Gorman, P. A. 2013, *Geophysical Research Letters*, 40, 4398, doi: [10.1002/grl.50796](https://doi.org/10.1002/grl.50796)
- Singh, M. S., & O’Neill, M. E. 2022, *Rev. Mod. Phys.*, 94, 015001, doi: [10.1103/RevModPhys.94.015001](https://doi.org/10.1103/RevModPhys.94.015001)
- Song, X., Abbot, D. S., & Yang, J. 2023, arXiv preprint arXiv:2307.01219
- Spaulding-Astudillo, F. E., & Mitchell, J. L. 2023, *Journal of the Atmospheric Sciences*,  
doi: [10.1175/JAS-D-22-0063.1](https://doi.org/10.1175/JAS-D-22-0063.1)
- . 2024, Data for Spaulding-Astudillo and Mitchell (2024a), "A simple model for the emergence of relaxation-oscillator convection", Zenodo,  
doi: [10.5281/zenodo.10982231](https://doi.org/10.5281/zenodo.10982231)
- Stevens, B., Giorgetta, M., Esch, M., et al. 2013, *Journal of Advances in Modeling Earth Systems*, 5, 146,  
doi: [10.1002/jame.20015](https://doi.org/10.1002/jame.20015)
- Sui, C.-H., Li, X., & Yang, M.-J. 2007, *Journal of the Atmospheric Sciences*, 64, 4506 ,  
doi: [10.1175/2007JAS2332.1](https://doi.org/10.1175/2007JAS2332.1)
- Sundqvist, H., Berge, E., & Kristjánsson, J. E. 1989, *Monthly Weather Review*, 117, 1641,  
doi: [10.1175/1520-0493\(1989\)117<1641:CACPSW>2.0.CO;2](https://doi.org/10.1175/1520-0493(1989)117<1641:CACPSW>2.0.CO;2)
- Tiedtke, M. 1989, *Monthly Weather Review*, 117, 1779,  
doi: [10.1175/1520-0493\(1989\)117<1779:ACMFSF>2.0.CO;2](https://doi.org/10.1175/1520-0493(1989)117<1779:ACMFSF>2.0.CO;2)
- Tokano, T. 2017, *Icarus*, 289, 120,  
doi: <https://doi.org/10.1016/j.icarus.2017.02.005>
- Tokano, T., McKay, C. P., Neubauer, F. M., et al. 2006, *Nature*, 442, 432, doi: [10.1038/nature04948](https://doi.org/10.1038/nature04948)
- Turtle, E. P., Perry, J. E., Hayes, A. G., et al. 2011, *Science*, 331, 1414, doi: [10.1126/science.1201063](https://doi.org/10.1126/science.1201063)
- Wolf, E., & Toon, O. 2013, *Astrobiology*, 13, 656,  
doi: [10.1089/ast.2012.0936](https://doi.org/10.1089/ast.2012.0936)
- Wolf, E. T., & Toon, O. B. 2015, *Journal of Geophysical Research: Atmospheres*, 120, 5775,  
doi: [10.1002/2015JD023302](https://doi.org/10.1002/2015JD023302)
- Wordsworth, R. D., & Pierrehumbert, R. T. 2013, *Astrophysical Journal*, 778,  
doi: [10.1088/0004-637X/778/2/154](https://doi.org/10.1088/0004-637X/778/2/154)
- Yang, D., & Seidel, S. D. 2020, *Journal of Climate*, 33, 2841 ,  
doi: <https://doi.org/10.1175/JCLI-D-19-0260.1>
- Yano, J.-I., & Plant, R. S. 2012, *Reviews of Geophysics*, 50,  
doi: <https://doi.org/10.1029/2011RG000378>
- Zhang, G., & McFarlane, N. A. 1995, *Atmosphere-Ocean*, 33, 407, doi: [10.1080/07055900.1995.9649539](https://doi.org/10.1080/07055900.1995.9649539)

## APPENDIX

## A. LIST OF PHYSICAL SYMBOLS, CONSTANTS, AND ACRONYMS

Symbol	Definition	Earth-like
$a$	Bulk-plume parameter	
$B$	Buoyancy ( $\text{m s}^{-2}$ )	
$c$	Condensation rate ( $\text{kg m}^{-3}\text{s}^{-1}$ )	
$c_p$	Specific heat of air at constant pressure ( $\text{J kg}^{-1}\text{K}^{-1}$ )	
$c_{pa}$	Specific heat of dry air at constant pressure ( $\text{J kg}^{-1}\text{K}^{-1}$ )	1006.04
$c_{pv}$	Specific heat of water vapor at constant pressure ( $\text{J kg}^{-1}\text{K}^{-1}$ )	1879
$\Delta(c_p T) + \Delta(gz)$	Dry static energy difference between the sub-cloud and cloud layer ( $\text{J kg}^{-1}$ )	
CAPE	Convective available potential energy ( $\text{J kg}^{-1}$ )	
$d$	Convective detrainment rate ( $\text{kg m}^{-3}\text{s}^{-1}$ )	
$e$	Convective entrainment rate ( $\text{kg m}^{-3}\text{s}^{-1}$ )	
$e^*$	Saturation vapor pressure of water (Pa)	
$f$	Frictional acceleration ( $\text{m s}^{-2}$ )	
$g$	Gravitational acceleration ( $\text{m s}^{-2}$ )	9.81
$h$ or MSE	Moist static energy ( $\text{J kg}^{-1}$ )	
$h_{sc}$	Moist static energy of the sub-cloud layer ( $\text{J kg}^{-1}$ )	
$h_{cl}$	Moist static energy of the cloud layer ( $\text{J kg}^{-1}$ )	
$\Delta h$	Moist static energy difference between the sub-cloud and cloud layer ( $\text{J kg}^{-1}$ )	
$h^*$	Saturation moist static energy ( $\text{J kg}^{-1}$ )	
$L$	Latent heat of vaporization of water ( $\text{J kg}^{-1}$ )	$2.5 \times 10^6$
$\Delta(Lq)$	Latent energy difference between the sub-cloud and cloud layer ( $\text{J kg}^{-1}$ )	
LCL	Lifting condensation level	
LNB	Level of neutral buoyancy	
LTRH	Lower-tropospheric radiative heating	
$LW_{toa}$	Top-of-atmosphere net longwave radiation ( $\text{W m}^{-2}$ )	
$LW_0$	Surface net longwave radiation ( $\text{W m}^{-2}$ )	
$M$	Convective mass flux ( $\text{kg m}^{-2}\text{s}^{-1}$ )	
$M_{sc}$	Sub-cloud mass flux ( $\text{kg m}^{-2}\text{s}^{-1}$ )	
PE	Precipitation efficiency	
$p$	Total atmospheric pressure (Pa)	
$P_s$	Surface precipitation rate ( $\text{kg m}^{-2}\text{s}^{-1}$ )	
$q$	Specific humidity ( $\text{kg kg}^{-1}$ )	
$q^*$	Saturation specific humidity ( $\text{kg kg}^{-1}$ )	
$Q_A$	Atmospheric radiative cooling ( $\text{W kg}^{-1}$ )	
$\overline{Q}_A$	Mass-integrated atmospheric radiative cooling ( $\text{W m}^{-2}$ )	
$\overline{Q}_{A,sc}$	Mass-integrated radiative cooling of the sub-cloud layer ( $\text{W m}^{-2}$ )	
$\overline{Q}_{A,cl}$	Mass-integrated radiative cooling of the cloud layer ( $\text{W m}^{-2}$ )	
$\overline{Q}_s$	Surface radiative heating ( $\text{W m}^{-2}$ )	
QE	Quasi-equilibrium	
$R_a$	Specific gas constant of dry air ( $\text{J kg}^{-1}\text{K}^{-1}$ )	287.04
$R_v$	Specific gas constant of water vapor ( $\text{J kg}^{-1}\text{K}^{-1}$ )	461
RH	Relative humidity	
RO	Relaxation oscillator	
$s$	Specific entropy ( $\text{J kg}^{-1}\text{K}^{-1}$ )	
$\dot{s}_{rad}$	Specific entropy change due to radiative processes ( $\text{J kg}^{-1}\text{K}^{-1}\text{s}^{-1}$ )	

$\dot{s}_{irr}$	Specific entropy change due to irreversible processes ( $\text{J kg}^{-1}\text{K}^{-1}\text{s}^{-1}$ )
$SW_{toa}$	Top-of-atmosphere net shortwave radiation ( $\text{W m}^{-2}$ )
$\Delta SW$	Shortwave radiation absorbed by the atmosphere ( $\text{W m}^{-2}$ )
SI	Vertically-integrated sink of water vapor from phase changes ( $\text{kg m}^{-2}\text{s}^{-1}$ )
$\bar{T}_A$	Mean temperature at which atmospheric radiation is emitted (K)
$1/\bar{T}_A$	Mean inverse temperature at which atmospheric radiation is emitted ( $\text{K}^{-1}$ )
$\bar{T}_{irr}$	Mean temperature at which frictional dissipation occurs (K)
$T_s$	Surface temperature (K)
$T_{trp}$	Tropopause temperature (K)
$v$	Air velocity ( $\text{m s}^{-1}$ )
$V$	Volume ( $\text{m}^3$ )
$\alpha$	Ratio of gross evaporation to gross condensation
$\delta$	Detrainment efficiency ( $\text{m}^{-1}$ )
$\varepsilon$	Entrainment efficiency ( $\text{m}^{-1}$ )
$\eta$	Efficiency of the convective heat engine
$\eta_{max}$	Maximum efficiency of the convective heat engine
$\gamma$	Water vapor lapse rate ( $\text{kg kg}^{-1}\text{m}^{-1}$ )
$\Gamma$	Temperature lapse rate ( $\text{K m}^{-1}$ )
$\rho$	Density of air ( $\text{kg m}^{-3}$ )
$\rho'$	Density of a plume/parcel ( $\text{kg m}^{-3}$ )

## B. DIAGNOSIS OF CONVECTIVE PARAMETERS: RESULTS AND INTERPRETATION

Figure 7 shows the mean temperature at which radiation is emitted from the atmosphere  $\bar{T}_A$ , the precipitation efficiency PE, the mean tropospheric relative humidity RH, and the bulk-plume parameter  $a$ , as diagnosed from the

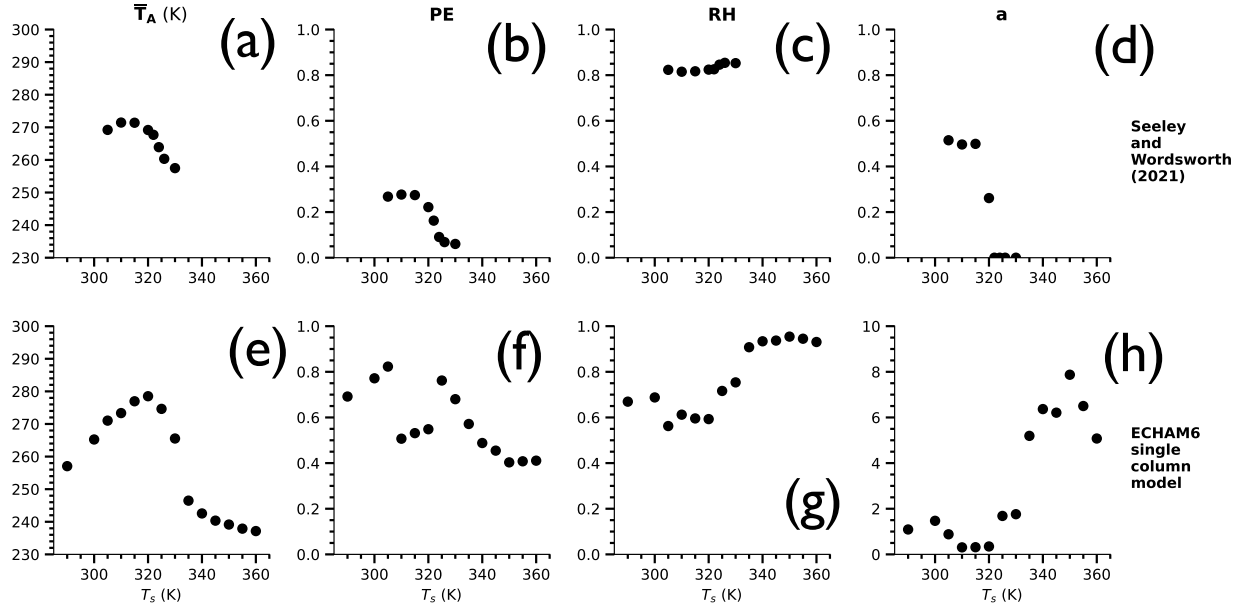


**Figure 7.** As a function of surface temperature, (a,e) mean temperature at which radiation is emitted,  $\bar{T}_A$ , (b,f) precipitation efficiency PE, (c,g) mean tropospheric relative humidity RH, and (d,h) bulk-plume parameter  $a$  from simulations with (a–d) a convection-resolving model (Seeley & Wordsworth 2021a) and (e–h) the ECHAM6 single-column model.

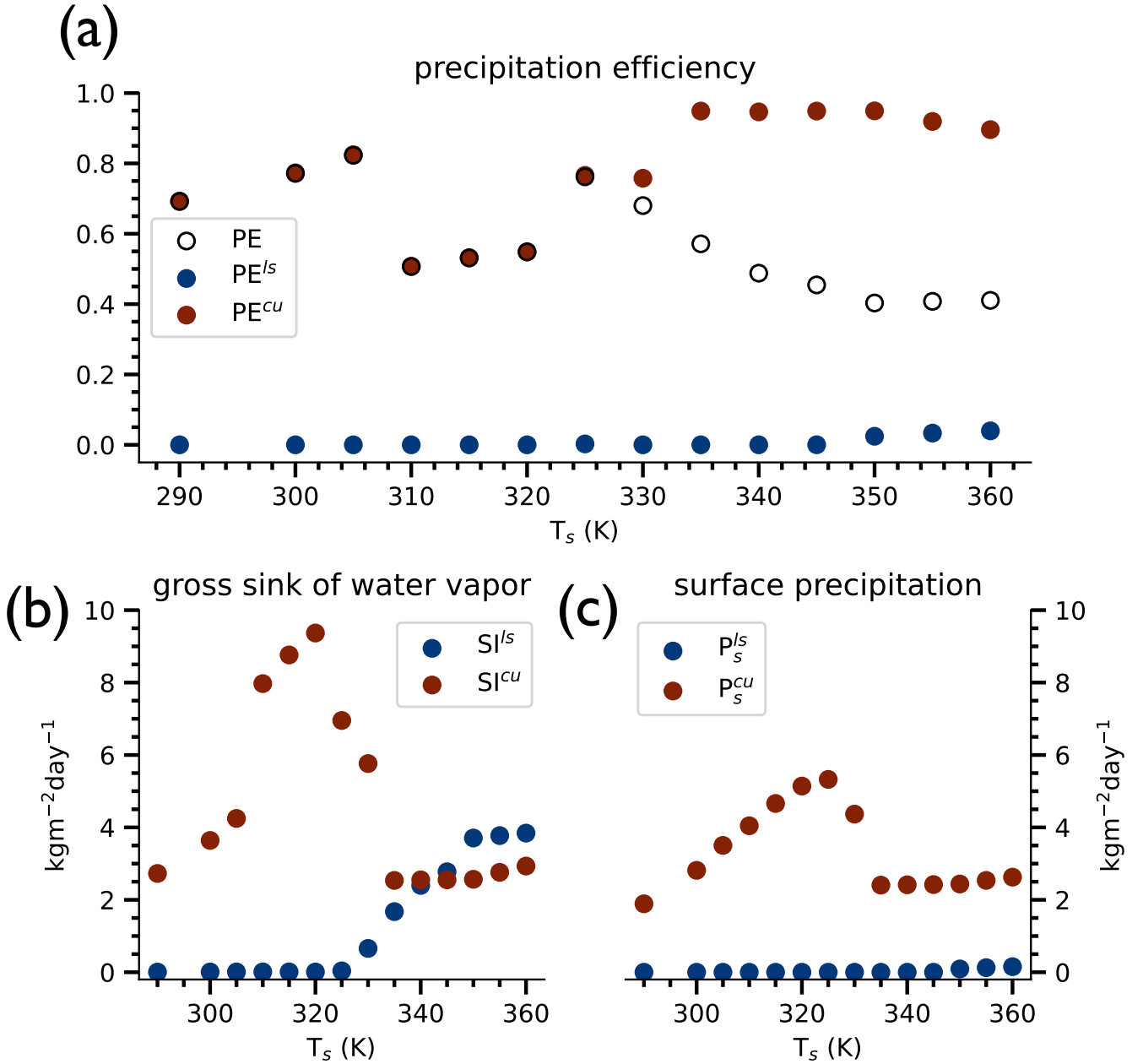


**Figure 8.** Diagnosed quantities from the ECHAM6 single-column model. (a) PE compared to the precipitation efficiency of the large-scale scheme  $PE^{ls}$  and the convection scheme  $PE^u$ . For visual clarity, PE is an unfilled marker. (b) Vertically-integrated gross sink of water vapor due to phase changes in the large-scale scheme  $SI^{ls}$  and the convection scheme  $SI^u$ . (c) Surface precipitation from the large-scale scheme  $P_s^{ls}$  and the convection scheme  $P_s^u$ .

convection-resolving simulations of [Seeley & Wordsworth \(2021a\)](#) and the ECHAM6 single-column model. Below, we discuss important trends and inter-model differences.

First, we consider the inter-model differences in PE (Figure 7b,f). Besides its relevance to the hydrological cycle, we care about PE because it allows us to diagnose *a*. The trend in PE with surface temperature in the convection-resolving model is not reproduced by the single-column model. In the convection-resolving model, PE takes values between 5-30%. The PE in the single-column model is substantially larger at all surface temperatures (up to a factor

of 10). To understand why, we diagnose the precipitation efficiencies of the large-scale and convection schemes in the single-column model separately. The convective and large-scale precipitation efficiencies are  $PE^u = P_s^u/SI^u$  and  $PE^{ls} = P_s^{ls}/SI^{ls}$  (see also Section 4.1.7). Note that these quantities are not strictly additive (i.e., they do not sum to PE). These separate metrics for precipitation efficiency, gross condensation, and surface precipitation are shown in Figure 8. Figure 8b reveals that there are two condensation regimes. For surface temperatures below 325 K, the majority of gross condensation in the atmosphere is convective in origin (Figure 8b). For this reason, PE is biased towards  $PE^u$  below 325 K (Figure 8a). Above 325 K, the fraction of gross condensation in updrafts decreases while the fraction of gross condensation in the large-scale environment increases, until the two are roughly equal in magnitude at 335 K (Figure 8b). Large-scale and convective sources of precipitation are displayed in Figure 8c, demonstrating that the latter dominates the total precipitation at every surface temperature. The bias of surface precipitation to the convection scheme is a well-documented behavior of general circulation models (Chen et al. 2021). Comparing the separate sources of gross condensation and surface precipitation, it is clear that the convection scheme is significantly more efficient than the large-scale scheme. Consistent with this interpretation,  $PE^u$  ranges from 50-100% and  $PE^{ls}$  is at most a few percent (Figure 8a). Lastly, there is a gradual decrease in PE between 325 to 350 K (Figure 8a). Figure 8b,c demonstrates that this decrease is related to the increasing fraction of gross condensation originating in the large-scale scheme, which biases the PE towards  $PE^{ls}$ .

Why is the convection scheme so much more efficient than the large-scale scheme in the single-column model? The answer lies in the parameterization design. In the convection scheme, a fraction of the condensates produced in updrafts are converted into convective precipitation. The rest is detrained into the environment, and is then converted into stratiform clouds or large-scale precipitation by the large-scale scheme. The large-scale precipitation is re-evaporated as it descends through the sub-saturated environment, but the convective precipitation is *assumed* to fall through the saturated updraft (this precludes re-evaporation of convective precipitation in the middle troposphere) and exits from the updraft base near the surface. This “insulation” of convective precipitation from environmental conditions within the plumes supports the persistent near-surface drizzle. In contrast, large-scale precipitation is exposed to sub-saturated environmental conditions during descent, which could explain why the overwhelming majority of gross condensates are re-evaporated before reaching the surface (Figure 8c). The difference in PE between the schemes is likely due to these assumptions. The convection-resolving model simulations tell us that the real PE should be closer to that of the large-scale scheme at high surface temperatures (Figures 7f and 8a). It might be possible to tune our

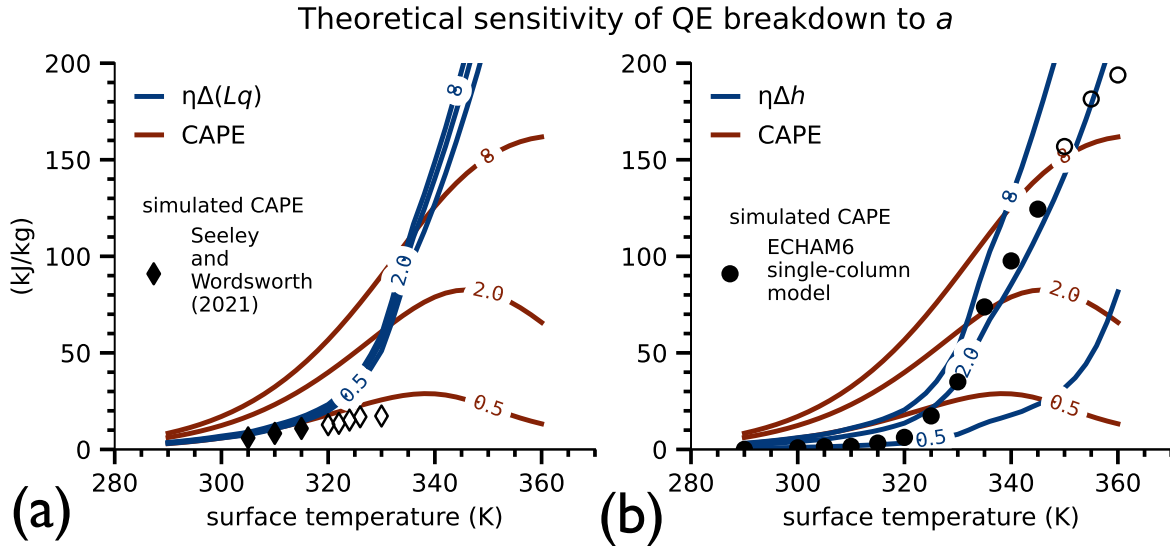


**Figure 9.** Sensitivity of the zero-buoyancy theory to varying the bulk-plume parameter  $a$ . The (solid) theoretical profiles are labeled by values of  $a$  between 0.5 and 8. We initialize the parcel at an assumed pressure of 1 bar, the temperature of the surface, and  $PE=25\%$ . In (a), we estimate the vertical heat transport as the vertical latent energy difference  $\Delta(Lq)$  only. The simulated CAPE from Seeley & Wordsworth (2021a) is plotted for reference (symbols). In (b), we estimate the vertical heat transport as the vertical moist static energy difference  $\Delta h$ . The simulated CAPE from the single-column model is plotted for reference. As in the main text, filled markers indicate QE states and unfilled markers indicate RO states.

model to have a lower PE at high temperatures in accordance with the convection-resolving simulations. We leave this as a future task, as the bias in the partitioning of rainwater in climate models is widespread (Chen et al. 2021) and beyond the scope of our work.

Using the PE (Figure 7b,f) and mean tropospheric RH from the simulations (Figure 7c,g), we are able to diagnose the bulk-plume parameter in both models.  $a$  is found to be less than 0.5 in the convection-resolving simulations on account of the high RH and low PE (Figure 7b,c). In the context of the zero-buoyancy theory (Section 2.2), this means that convective plumes and environmental air are moderately coupled.  $a$  is substantially larger in the single-column model; it ranges from 0.3-1.5 below 325 K and from 1.5-8 above 325 K (Figure 7h). There is a significant increase in  $a$  above 325 K (Figure 7h) related to the decline in PE, rather than the increase in RH (the latter would act to reduce  $a$ ). Figure 9 shows the effect of varying  $a$  between 0.5-8 on the theoretical CAPE. In general, larger values of  $a$  support more steady-state storage of CAPE (e.g., Figure 9a). Low values of  $a$  give a better fit to the convection-resolving model simulations (Figure 9a), as might be expected from Figure 7d. Conversely,  $a = 8$  yields values for CAPE that approach those observed at high surface temperatures in the single-column model (Figure 9b).

Interestingly, the theoretical temperature of QE breakdown is sensitive to the value of  $a$  (Figure 9b). We are interested in this sensitivity as a potential explanation for the 30 K difference in the surface temperature of RO emergence between the models. As you increase  $a$ , the temperature of QE breakdown decreases (Figure 9b). Why is this? The dry static energy has a strong dependence on  $a$  in the theory because of the location of the minimum in tropospheric MSE. In the zero-buoyancy theory, decreasing  $a$  reduces the lapse rate, which causes the MSE minimum to rise to a higher elevation. This means that the dry static energy difference becomes more negative (and therefore reduces  $\Delta h$ ) with decreasing  $a$ . That  $a$  is larger in the single-column model does not seem to explain why the RO state emerges at a lower surface temperature in the convection-resolving model.

However, the theoretical prediction for QE breakdown is sensitive to the method of estimating vertical heat transport. In this study, we chose to use a simple difference of the MSE between the surface and the tropospheric minimum value. Consider the scenario in Figure 9a where  $\Delta h$  is approximated by the latent energy  $\Delta(Lq)$ . In this case where we have neglected the vertical dry static energy difference, the temperature of QE breakdown is instead found to *increase* with increasing  $a$ . This result is more consistent with our intuition, and leads us to suspect that there is a better way to estimate the vertical heat transport. Future work should therefore interrogate our assumptions about the vertical heat transport in an atmosphere with zero buoyancy. We assumed that upward air records the MSE near the surface and downward air records the minimum in MSE, but is that consistent with zero buoyancy? The environmental temperature and moisture profile in the zero-buoyancy model is a reflection of the mutual interaction (entrainment, detrainment, re-evaporation) between ascending and descending air, which differs only in terms of moisture content. In this process, air parcels exchanged across the same level have the same dry static energy, and differ only in their moisture content. This might mean that the appropriate measure of vertical heat transport in the zero-buoyancy atmosphere is not  $\Delta h$ , but rather  $\Delta(Lq)$  or some variant thereof.

### C. HOW TO CALCULATE CAPE IN THE SIMULATIONS

This appendix summarizes our process of calculating CAPE in the simulations (Romps 2008, 2015; Marquet 2016; Emanuel 1994). To ensure consistency in our analysis, we apply the same parcel methods to the data from the convection-resolving model of Seeley & Wordsworth (2021a) and our single-column model.

Moist air is defined to be a mixture containing dry air and water in various phases. The mass fraction (i.e. specific humidity) is represented by the symbol  $q_x$ .  $x$  is a generic subscript referring either to dry air  $a$ , water vapor  $v$ , liquid water  $l$ , or solid ice  $s$ . The mixing ratio is represented by the symbol  $r_x$ , and is related to the specific humidity by  $r_x = q_x/q_a$ . The density of dry air is  $\rho_a = p_a/(R_a T)$ . The partial pressure of dry air in the parcel is a function of the total pressure  $p$  (given by the simulation) and the water vapor mixing ratio  $r_v$ :

$$p_a = p(1 + r_v/\epsilon)^{-1}, \quad (C1)$$

where  $\epsilon = R_a/R_v$ . When the specific volume of liquid and solid phases of water are neglected, the density of the moist air parcel is (Emanuel 1994)

$$\rho = \frac{p}{R_a T} \frac{1 + r_t}{1 + r_v/\epsilon}, \quad (C2)$$

where  $r_t = r_v + r_l + r_s$  is the total mixing ratio of water. For simplicity, we will ignore the solid phase ( $r_s, q_s = 0$ ) in our parcel calculations and assume that, regardless of temperature, condensed water exists only in the liquid phase;

however, we will retain variables associated with ice in subsequent equations for reader clarity. The saturation vapor pressure over liquid is (Romps 2008, 2015)

$$e^{*,l} = p_{trip} \left( \frac{T}{T_{trip}} \right)^{(c_{pv}-c_{vl})/R_v} \times \exp \left[ \frac{E_{0v} - (c_{vv} - c_{vl})T_{trip}}{R_v} \left( \frac{1}{T_{trip}} - \frac{1}{T} \right) \right], \quad (C3)$$

where  $p_{trip} = 611.65$  Pa and  $T_{trip} = 273.16$  K are the triple point pressure and temperature,  $c_{pv} = 1879$  Jkg<sup>-1</sup>K<sup>-1</sup> is the isobaric specific heat of water vapor,  $c_{vv} = 1418$  Jkg<sup>-1</sup>K<sup>-1</sup> and  $c_{vl} = 4119$  Jkg<sup>-1</sup>K<sup>-1</sup> are the isochoric specific heats of water vapor and liquid water, and  $E_{0v} = 2.374 \times 10^6$  Jkg<sup>-1</sup> is the difference in specific internal energy between water vapor and liquid water at the triple point temperature (Romps 2015). The saturation specific humidity over liquid is then given by

$$q^{*,l} = \frac{\rho_v^*}{\rho} = \frac{R_a}{R_v} \frac{e^{*,l}}{p} \frac{1 + r_v/\epsilon}{1 + r_t} \quad (C4)$$

To determine the lapse rate of an “adiabatic parcel”<sup>16</sup>, we invoke the conservation of the sum of MSE and CAPE (Marquet 2016; Romps 2015): that is, MSE + CAPE. Taking the vertical derivative of this conserved quantity and using the definition of CAPE,

$$\frac{\partial \text{MSE}}{\partial z} = -\frac{\partial}{\partial z} \int_{z_{lcl}}^z B(z') dz' = -B(z) \quad (C5)$$

where

$$\text{MSE} = [q_a c_{pa} + (q_v + q_l + q_s) c_{vl}] (T - T_{trip}) + q_v L_c - q_s L_f + g z. \quad (C6)$$

$z_{lcl}$  is the height of the lifting condensation level,  $c_{pa}$  is the isobaric specific heat of dry air,  $L_c = E_{0v} + R_v T + (c_{vv} - c_{vl})(T - T_{trip})$  is the latent heat of condensation, and  $L_f = E_{0s} + (c_{vl} - c_{vs})(T - T_{trip})$  is the latent heat of fusion.  $c_{vs} = 1861$  Jkg<sup>-1</sup>K<sup>-1</sup> is the isochoric specific heat of solid water, and  $E_{0s} = 3.34 \times 10^5$  Jkg<sup>-1</sup> is the difference in specific internal energy between water liquid and solid at the triple point temperature (Romps 2015).

For detailed instructions on how to obtain the temperature and density profile of an adiabatic parcel with the same pressure as the local environment using conservation of MSE+CAPE, we refer the reader to Romps (2015). However, we do offer a short summary below. MSE and  $B$  at height  $z$  depend on  $T$  and  $q_x$ . The MSE at  $z + \Delta z$  follows from Equation C5. Solving for the parcel temperature at  $z + \Delta z$  from the MSE (Equation C6) requires a root solver. The reason is that MSE is a function of both temperature and the water mass fraction, where the partitioning between vapor, liquid, and solid phases is itself temperature-dependent. The solution constraints are that the vapor phase must remain pegged to the saturation value above the LCL and total moisture must be conserved during each discrete lifting step. When the level of neutral buoyancy is reached, the buoyancy  $B(z)$  can be integrated upward from the LCL to yield CAPE.

We have thus far detailed the parcel method for reversible ascent, where the total water in the parcel is conserved. We now discuss how to approach lifting scenarios where total moisture is not conserved, such as pseudo-adiabatic ascent.

### C.1. Ascent with condensate removal

An example of irreversible ascent is where the condensed moisture in the parcel is removed in part or in whole (i.e., pseudo-adiabatic). This process usually carries away a small amount of mass. The changing mass of the parcel produces a change in the specific humidity, which is accounted for as follows. The initial mass of the parcel is  $m_{tot}^i = m_a^i + m_v^i + m_l^i + m_s^i$ . The superscripts  $i$  and  $f$  are used to track the initial and final state of the parcel. For simplicity, we only detail the treatment of liquid removal, but note that ice removal would proceed analogously. Condensate removal is parameterized as exponential decay following Seeley & Wordsworth (2023):

$$\frac{\partial q_l}{\partial z} = -q_l/L \quad (C7)$$

<sup>16</sup> Here, “adiabatic” refers to any parcel that is raised without exchanging heat or mass with its surroundings, irrespective of the assumptions about moisture removal in the lifting method. For pseudo-adiabatic ascent, we remove all moisture after each discrete lifting step. For reversible ascent, the total moisture is conserved during and after the lifting step.



where  $L$  is a characteristic length scale. Suppose that we remove a mass of liquid water  $\Delta m_l < 0$  as prescribed by Equation C7. The final and initial masses are related by  $m_a^i = m_a^f$ ,  $m_v^i = m_v^f$ , and  $m_l^f = m_l^i + \Delta m_l$ , where we have neglected ice. The final mass fraction for dry gas and water vapor are

$$q_a^f = \frac{m_a}{m_{tot}^i + \Delta m_l} = \frac{q_a^i}{1 + \Delta q_l} \quad \text{and} \quad q_v^f = \frac{m_v}{m_{tot}^i + \Delta m_l} = \frac{q_v^i}{1 + \Delta q_l}. \quad (\text{C8})$$

where in the second step we divided through by  $m_{tot}^i$ . The liquid removal step increases the mass fraction of dry gas and vapor by a factor of  $(1 + \Delta q_l)^{-1}$ . The final mass fraction for liquid water is

$$q_l^f = \frac{m_l^f}{m_{tot}^f} = \frac{m_l^i + \Delta m_l}{m_{tot}^i + \Delta m_l} = \frac{q_l^i + \Delta q_l}{1 + \Delta q_l}, \quad (\text{C9})$$

where we have accounted for the changing total mass in addition to the total mass of liquid water. This method can be used to evaluate lifting processes from fully reversible ( $L \rightarrow \infty$ ) to pseudo-adiabatic ( $L \rightarrow 0$ ). The final mass fractions are used to update the parcel buoyancy and MSE before the next discrete lifting step.